Aerodynamic simulation of rotating wheels in a solar car

Kristof BORGIONS

Thomas HOLEMANS

Acknowledgements

Samenvatting

Het KU Leuven Solar team strijdt elke twee jaar voor de eerste plaats in de Bridgestone World Solar Challenge. Het team dingt mee naar de titel in de 'Challenger' categorie, deze competitie gaat over snelheid. Voor elke race ontwikkelen zij een ultra-low drag voertuig aangedreven door zonne-energie. Ieder jaar proberen ze beter te zijn dan het jaar voordien door een sterke focus op de luchtweerstand van het voertuig. Dit gebeurt voornamelijk via CFD-simulaties om de stroming rond de wagen te modelleren en uiteindelijk ook door het uitvoeren van windtunneltesten. Tot nog toe werden alle CFD-simulaties uitgevoerd zonder de wielen mee in rekening te brengen om de bijhorende rekentijd haalbaar te houden. De windtunneltesten worden wel uitgevoerd met de wielen maar deze staan stil omdat de gebruikte windtunnel geen bewegende ondergrond ter beschikking heeft. Omdat de wielen een significante invloed hebben op de aerodynamica, bestudeert deze thesis de invloed van de roterende wielen op de aerodynamica van de Punch Two solar car van het KU Leuven solar team. Rijomstandigheden worden gemodelleerd met een bewegende grond en roterende wielen. Deze situatie wordt vergeleken met een bewegende grond en stilstaande wielen. Het vergelijken van deze twee scenario's maakt het mogelijk om de invloed van roterende wielen ten opzichte van stationare wielen op de stroming te vergelijken. Een belangrijk aspect van dit onderzoek is om de rekentijd tot een minimum te beperken. Met een lage rekentijd is het mogelijk voor toekomstige Solar teams om de uiteindelijke wagen met roterende wielen te modelleren.

Indien dit, door tijdsbeperking, niet meer mogelijk is, kan het team het in dit onderzoek opgestelde model gebruiken om de resultaten van hun simulatie/windtunneltest te projecteren naar een resultaat waar er wel roterende wielen aanwezig zijn.

Extended Abstract

The KU Leuven solar team aims every two years at the first place in the Bridgestone World Solar Challenge. For this race, an ultra-low-drag vehicle powered by solar energy is designed. They aim to get each new car better than the previous one. In order to reach this goal, there is a strong focus on reducing the drag. This is done by using CFD to model the flow around the car and by testing the car in a wind tunnel. Till now, all CFD simulations were performed without the wheels because of predicted unsteady behaviour or time shortage. The wind tunnel tests are performed with stationary wheels because the infrastructure is not capable of rotating the wheels. This means that neither the simulations nor the wind tunnel tests represent real-life conditions, namely rotating wheels.

This research investigates the influence of rotating wheels on the Punch Two solar car of the KU Leuven Solar Team. The real-life case will be modelled with a moving ground and rotating wheels, which will be compared to a moving ground and stationary wheels, this method allows us to isolate the influence of the rotation from other factors. The focus of this research has also been to keep the computation time as low as possible. With a low computation time, it would be possible for the future Solar Teams to model the car with rotating wheels. If time is insufficient for the team, they could use the results of this research to project their results to a result with rotating wheels. The previous thesis about the Punch Two was devoted to finding the best turbulence model for this car, this research performed by Uten and Vandervelpen [1] concluded that k-ω SST is the best RANS model of the models tested. Their conclusion is greatly adopted in this research and therefore the k-ω SST model is the used turbulence model used in this research. The rotation of the wheels is modelled by a Moving Wall boundary condition. This method is suitable for the solar car wheels because the rim lacks spokes and it will lead to a decrease in computational time. From our research follows that adding rotation to the wheels, at 90kmph, lowers the drag of the wheels by 41.43%. This is because stationary wheels show vortex shedding, whereas rotating wheels suppress it. The pressure drag is mainly affected, this not only changes in size but also in periodicity and amplitude of vortex shedding. The viscous drag isn't much affected by the rotation, it only drops 1.33%. The total average drag of the car drops by 9.54%, the vortex shedding frequency changes with 7.99Hz (38.52%) and the amplitude of the vortex shedding drops by 95.85%. Besides defining the differences in drag between rotating and stationary wheels, this research visualises the flow field of the wheels and their influence on the flow field of the car. This visualisation can be used to perform tactical improvements to the wheel housing and/or guide the flow behind the wheels. These improvements are left for further

research, for which this research can be a basis. The simulation with stationary wheels showed interesting behaviour which could suggest that the wheels create a beat. This would mean that the frequency of vortex shedding of the front and back wheel are different. Further research into this behaviour would be an interesting topic.

All the modelling and calculations will be done using CFD software provided by NUMECA. The complete setup of the mesh, as well as the solver will be thoroughly discussed, this should aid future research to the flow of rotating wheels for the KU Leuven solar cars.

Keywords: Aerodynamic Drag, CFD, KU Leuven Solar car, Moving wall boundary condition, RANS, Rotating wheels

Contents

List of Figures

List of Tables

List of symbols

A	:	surface area	$[m^2]$
C	:	Courant number	
C_d	:	the drag coefficient	
dt	:	timestep	$[s]$
$\frac{du}{dy}$	:	velocity gradient normal to the surface	$[1/s]$
dx	:	length interval	$[m]$
f	:	frequency of vortex shedding	$[Hz]$
g	:	gravitational acceleration	$[m/s^2]$
k	:	turbulence kinetic energy	$[m^2/s]$
n	:	number of viscous layers	
o	:	order of convergence	
p	:	pressure	$[N/m^2]$
r	:	refinement ratio	
s	:	variable for which convergence study is performed	[N or Hz]
t	:	time	$[s]$
u	:	local velocity	$[m/s]$
u_t	:	friction velocity	$[m/s]$
u_x	:	x component of velocity	$[m/s]$
u_y	:	y component of velocity	$[m/s]$
u_z	:	z component of velocity	$[m/s]$
v	:	kinematic viscosity	$[m^2/s]$
x_{inlet}	:	streamwise distance between inlet wind tunnel and computational domain	$[m]$
x, y, z	:	unity spatial vectors	
y	:	absolute distance from the wall	$[m]$
y^+	:	dimensionless wall distance	
y_{wall}	:	first layer thickness	$[m]$
C_μ	:	0.09 (constant)	
GCI	:	Grid Convergence Index	[%]
L	:	characteristic length of object	$[m]$
Re	:	Reynolds number	
SCS	:	surrounding cell size	[m]

SR	:	stretching ratio	
St	:	Strouhal number	
T_u	:	turbulence intensity at inlet computational domain	$[\%]$
$T_{u,inlet}$	:	turbulence intensity at inlet wind tunnel	$[\%]$
U	:	free stream velocity	$[m/s]$
β	:	0.09 (constant)	
β^*	:	0.0828 (constant)	
ε	:	rate of dissipation of turbulence energy	$[m^2/s^3]$
μ	:	dynamic viscosity	$[Pa \cdot s]$
μ_t/μ	:	turbulence viscosity ratio	
ρ	:	density	$[kg/m^3]$
τ	:	shear stress	$[N/m^2]$

List of abbreviations

avg	:	Average
CAD	:	Computer-Aided Design
CFD	:	Computational Fluid Dynamics
CPU	:	Central Processing Unit
D	:	Diameter
DES	:	Detached Eddy Simulation
DNS	:	Direct Numerical Design
GCI	:	Grid Convergence Index
H	:	Height
L	:	Length
LES	:	Large Eddy simulation
min	:	Minimum
max	:	Maximum
MRF	:	Moving reference frame
MW	:	Moving wall
RANS	:	Reynolds Averaged Navier Stokes
SCS	:	Surrounding cell size
SR	:	Stretching ratio
SST	:	Shear Stress Transport
W	:	Width

Chapter 1

Introduction

1.1   Nature of the problem

The design of aerodynamic features is crucial for a competitive race car. Aerodynamic effects are equally important to a vehicle as its top speed, handling and available engine power [2]. Parallel to this, one can conclude that for a solar car the aerodynamic effects will have a significant impact on the performance of the solar car both in speed, handling and endurance. The aerodynamics of every solar car produced by Solar Team KU Leuven has been researched, and after every research the design has been improved. These improvements are made to aim at the first place in the Bridgestone world solar challenge at which the solar car participates every two years. Until now, none of these studies have considered the influence of the rotating wheels on the aerodynamics. There are two main reasons for this constant neglect of the wheels. First of all, there is little research on the aerodynamic behaviour of rotating wheels which would create a complex flow. This means that it would take a lot of time to simulate this behaviour and this must be done after they have designed the body of the car which is already a time-consuming part. Secondly, the wind tunnel where they test their cars is not able to rotate the wheels, so they don't have a reference to check the simulation results. Till now, most aerodynamic simulations have been made neglecting the wheels, even though these wheels could alter the flow. To optimise the wheel arch as well as certain parts of the car itself, it is important to understand the airflow around the wheels and the influence of the wheels on the total flow. Even though there are no regulations about computational time or wind-tunnel testing as in many other competitions, the CPU computational time is still an important parameter in the research because of the limited time and CPU power that is available to the team [3].

1.2   Goal of the research

The goal of the study is to investigate how the wheels, and especially the rotation of the wheels, alter the flow around the car and how this influences the drag. For this, the flow around the car and the wheels will be modelled using CFD software. The results from the previous research of

Emmerick Vandervelpen and Joachim Uten [1], which analysed the car without the wheels, will serve as a starting point. Eventually, the goal is to find a model to predict the change in drag due to the rotating wheels. To reach this goal, a theoretical study, of previous cases, will be performed and CFD software provided by NUMECA will be used to model the flow. [4]

1.3 Outline of the paper

Chapter 1 contains the introduction to this paper, including the nature of the problem and the goal of the research. In chapter 2, this paper explains theory about aerodynamic concepts. This is to make sure enough information is available to understand the continuation of this paper. Chapter 3 is an analysis of current researches about the topic, namely rotating wheels. Conclusions and advice from these researches are adopted in this paper. In chapter 4, the mesh generation is discussed. In this chapter, a detailed description is given on the generation of the mesh, as well as an analysis of the quality. Chapter 5 describes the derivation of the different solver settings. In chapter 6, the results of this research are described. This chapter starts with a verification and validation of the results which is an important part in CFD simulations. After that, the influence of rotation on the drag is discussed and this chapter ends with a flow field visualisation. To finalise this paper, Chapter 7 summarises the conclusions and proposes further research on the the topic of this paper.

Chapter 2

Theory

2.1 Computational Fluid Dynamics (CFD)

Computational fluid dynamics or CFD made a rise in popularity together with the increasing computational power available. This is mainly because CFD helps in the design stage without the need for real prototypes, thus it will reduce the number of test runs, as well as time in windtunnels, resulting in reduced costs. As we will see in section 2.2.1, a flow can be fully described by the Navier-Stokes equations. Theoretically, these equations can be solved if there is enough information about the initial and boundary conditions. In practice, except for very simple problems, there is no analytic solution. This is because the unknowns are present in every equation and therefore the equations have to be solved simultaneously. Also, the equations consist of non-linear terms which require an iterative way of solving them. Moreover, the fact that they are of a second-order partial differential equation makes it harder to solve. All of this makes it currently impossible to solve these equations analytically. This is the reason we have to use CFD simulations. With CFD the continuous domain will be divided into discrete points, called a mesh or a grid, and the differential equations will be solved numerically [5]. This will lead to a solution but will also introduce errors because CFD is not calculating the actual, continuous domain. In CFD there are three main errors: the discretisation, the numerical and the modelling error. The discretisation error is because of the division into discrete points. A finer grid will be able to capture the geometry in a better way and it will also be able to compute smaller phenomena occurring in the flow. This will result in a more exact solution, but it needs more computational power and thus more time. This leads to the biggest compromise in CFD-simulations: accuracy against time. The numerical error is a round-off error. This error increases when the grid is finer because it needs more iterations to solve, causing numerical errors to grow. Also small and big values in the equations (for example due to a bad mesh) cause bigger numerical errors. The physical modelling error arises because of the uncertainty in the formulation of the chosen turbulence model, which will be discussed later on. Because of the time problem, there is a lot of research on approximating the flow by models instead of calculating the entire flow. When computing turbulence, the scales are very small. Therefore, we will use turbulence models. Every model has its own set

of equations, which are based on empirically derived coefficients. These models will introduce extra errors. An important part of our research will be to keep these errors to a minimum, reach the desired accuracy and do it in an efficient way by keeping the computational time as low as possible.

2.2 Aerodynamics

To understand the further research in this thesis, it is important to understand some of the principles of aerodynamics. First of all, the Navier-Stokes equations, which describe a flow analytically, will be discussed. After that, the concept of boundary layer and boundary layer separation will be explained. Next, turbulence and ways of modelling turbulence will be discussed. Finally, the types of drag that the solar car experiences will be discussed, as well as ways to minimise this drag.

2.2.1 Navier-Stokes equations

The Navier-Stokes equations (2.1, 2.2, 2.3 and 2.4) describe the behaviour of a fluid. In total, the Navier-Stokes equations consist out of four equations. The first equation describes the conservation of mass. The following three describe the conservation of momentum in each direction of space. The Navier-Stokes equations for incompressible, Newtonian fluids are [6]:

$$\frac{\partial u_x}{\partial x} + \frac{\partial u_y}{\partial y} + \frac{\partial u_z}{\partial z} = 0 \tag{2.1}$$

$$\rho\left(\frac{\partial u_x}{\partial t} + u_x\frac{\partial u_x}{\partial x} + u_y\frac{\partial u_x}{\partial y} + u_z\frac{\partial u_x}{\partial z}\right) = \rho g_x - \frac{\partial p}{\partial x} + \mu\left(\frac{\partial^2 u_x}{\partial x^2} + \frac{\partial^2 u_x}{\partial y^2} + \frac{\partial^2 u_x}{\partial z^2}\right) \tag{2.2}$$

$$\rho\left(\frac{\partial u_y}{\partial t} + u_x\frac{\partial u_y}{\partial x} + u_y\frac{\partial u_y}{\partial y} + u_z\frac{\partial u_y}{\partial z}\right) = \rho g_y - \frac{\partial p}{\partial y} + \mu\left(\frac{\partial^2 u_y}{\partial x^2} + \frac{\partial^2 u_y}{\partial y^2} + \frac{\partial^2 u_y}{\partial z^2}\right) \tag{2.3}$$

$$\rho\left(\frac{\partial u_z}{\partial t} + u_x\frac{\partial u_z}{\partial x} + u_y\frac{\partial u_z}{\partial y} + u_z\frac{\partial u_z}{\partial z}\right) = \rho g_z - \frac{\partial p}{\partial z} + \mu\left(\frac{\partial^2 u_z}{\partial x^2} + \frac{\partial^2 u_z}{\partial y^2} + \frac{\partial^2 u_z}{\partial z^2}\right) \tag{2.4}$$

where:

u_x	:	x component of velocity	$[m/s]$
u_y	:	y component of velocity	$[m/s]$
u_z	:	z component of velocity	$[m/s]$
x, y, z	:	unity spatial vectors	
t	:	time	$[s]$
ρ	:	density	$[kg/m^3]$
g	:	gravitational acceleration	$[m/s^2]$
p	:	pressure	$[N/m^2]$
μ	:	dynamic viscosity	$[Pa \cdot s]$

The foundation of the momentum equations is the second law of Newton which states that $dm \cdot \frac{dv}{dt} = \sum F$: acceleration of a mass is defined by the forces acting on it. In the momentum equations, the left part is equal to mass times acceleration and the right part is the summation of the forces. This equation can be filled in with all the forces acting on a infinitesimally small volume. The forces on this volume are the normal stresses (σ) and the shear stresses (τ) multiplied by the surface they are acting on as well as the gravitational force. The different stresses are shown on one plane on figure 2.1.
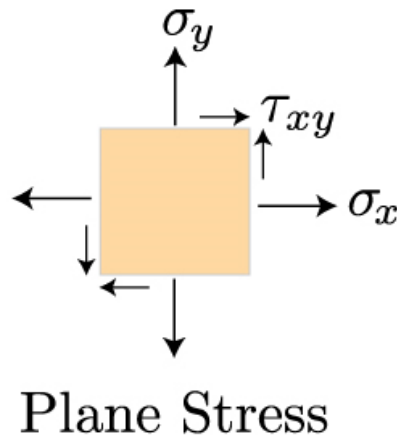
Figure 2.1: Stresses on one plane, [7]

The shear stresses can be described in function of the viscosity and the velocity gradients. The normal stresses can be described in function of the pressure. This results in the final equations which are describing the velocities u_x, u_y, u_z and pressure p in function of space x,y,z and time t. To use these equations, it is required that the fluid is Newtonian (constant viscosity) and incompressible [5]. For our application, this is valid because air can be considered Newtonian and incompressible below speeds of Mach 0.3.

2.2.2 Boundary Layer

The boundary layer is an important characteristic when studying aerodynamic properties. This paragraph will explain what the boundary layer is, what types of boundary layers exist and examine the separation of a boundary layer.

Properties

On figure 2.2, a boundary layer is shown. The no-slip condition states that a viscous fluid will stick to the surface of an object. Thus, the relative velocity between the fluid and the boundary of an object will be zero [8]. Between this stationary fluid layer and relatively moving layers above it, shear stresses arise, causing these moving layers to slow down. These shear stresses are equal to:

$$\tau = \mu \frac{du}{dy} \tag{2.5}$$

where:

$\frac{du}{dy}$	:	velocity gradient normal to the surface	$[1/s]$
τ	:	shear stress	$[N/m^2]$

Due to these viscous shear stresses between fluid layers, a gradual change in velocity will arise away from the boundary. From a certain distance away from the surface of the body, the velocity stays the same and there is no influence anymore of the body to the fluid. The transition layer where the velocity changes relatively from standstill to the external speed. This transition layer of relative velocity zero to the external velocity is called the boundary layer. The boundary layer gives a body an effective aerodynamic shape. The viscosity of the fluid is an important parameter for the boundary layer. When the viscosity is higher, the forces between the fluid layers will be higher which will result in a lower velocity gradient. From this one can conclude that the viscosity has an influence on the thickness of the boundary layer. [8]

There are three types of boundary layers: laminar, transitional and turbulent. With a laminar boundary layer, there are clear velocity layers. These can be solved with the Navier-Stokes equations. When the flow is turbulent, the flow cannot be fully solved because the small scale phenomena are too small which would require too much computational power. Therefore, turbulence models are used (discussed in 2.2.4). In the fully turbulent boundary layer, there are 3 regions: the viscous sublayer, the buffer layer and the turbulent region. The viscous sublayer has a relatively small Reynolds number in comparison with the other layers. In this layer, the viscous effects dominate over the turbulent ones. It can be seen as a laminar sublayer where the velocity is linear with the height. Above this layer is the buffer layer. Here, turbulent stresses start to dominate over the viscous ones till it is fully turbulent. The viscous sublayer and buffer layer are very small in comparison to the turbulent region (+- 100 times smaller) [5]. The various layers can be seen on figure 2.2.
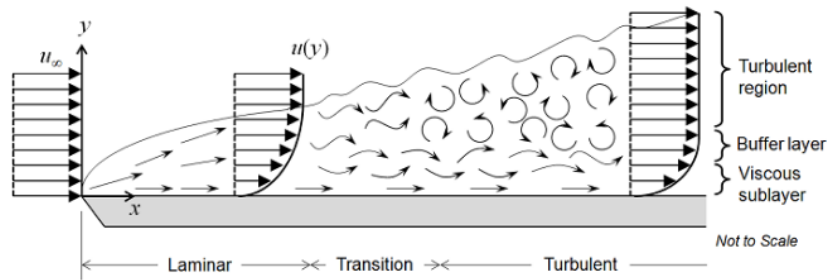
Figure 2.2: Different types of boundary layer, [9]

An important parameter describing these different layers, is the y^+ value:

$$y^+ = \frac{y \cdot u_t}{v} \tag{2.6}$$

where:

y^+	:	dimensonless wall distance	
y	:	absolute distance from the wall	$[m]$
u_t	:	friction velocity	$[m/s]$
v	:	kinematic viscosity	$[Pa \cdot s]$

y^+ is a normalised, non-dimensional quantity that is the same for every boundary layer. This quantity tells us in which layer of the boundary layer the flow is situated (viscous sublayer, buffer layer, turbulent layer). It could be seen as a local Reynolds number for the boundary layer.
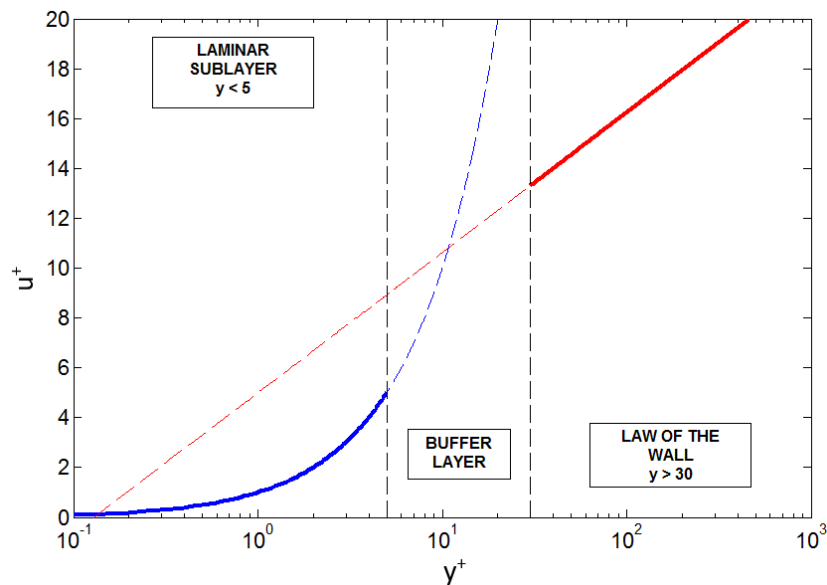
Figure 2.3: y^+ in function of u^+ in boundary layer, [10]

y^+ in function of u^+ can be seen on figure 2.3. At low y^+ values, y^+ is linear to u^+ (blue line). At higher values it has a logarithmic relation (red line). Between these two parts, the buffer layer is situated which is an unknown region. The different types of modelling this near-wall flow will be discussed in section 2.2.5.

The boundary layer thickness is another important property of the boundary layer. It is dependent on different factors, which will be briefly discussed:

- **Length of the object**, the boundary layer becomes thicker downstream (as seen on figure 2.2). Because of the shear stresses inside the boundary layer, there will be losses in the form of heat, slowing down the particles inside the boundary layer. This slowing down will affect the flow layers above and slow them down as well, causing the boundary layer to grow.

- **Free stream velocity**, when the velocity increases, the boundary layer becomes smaller. This is because the viscosity of the fluid will have a smaller impact compared to the higher inertial forces and it will not be able to slow down as much fluid as with lower speeds.

- **Viscosity**, a fluid that has a higher viscosity will have higher shear stresses and thus slow down more fluid, increasing the boundary layer thickness.

- **Turbulence**, a turbulent boundary layer will grow more rapidly than a laminar one. This is because the chaos and rotation of a fluid due to the turbulence will affect the upper layers more than a laminar one. Also, there will be more dissipation of energy.

- **Pressure gradient**, as we will see below in section 2.2.2, a curved object will generate a pressure gradient along its surface. An adverse pressure gradient, will slow down the fluid and thus increase the boundary layer thickness.

As we have seen above, the boundary layer can be laminar, transitional or turbulent. In section 2.2.4 we will see that turbulence arises from small distortions or instabilities in the flow. These instabilities can be amplified by a higher velocity or dampened out by the viscosity as we will see later on. For now, we will focus on the origin of instabilities in the boundary layer to be able to tackle these problems later on when studying the drag. First of all, a thicker boundary layer is less stable than a small one and will more likely become turbulent. This is because the momentum of the instabilities, related to the surface, becomes larger with a larger boundary layer. That's why the flow might transition from laminar to turbulent further downstream an object even when there are no other instabilities. Another factor is the roughness of the surface. A rough surface will cause more instabilities and thus encourage turbulence. Again, the pressure gradient might cause instabilities in the boundary layer. This is because a high enough adverse pressure gradient will cause backflow, and this will introduce instabilities. Finally, the streamlining of the object will cause fewer oscillations. When the incoming, free stream flow can go around the surface in a smooth way, it will cause fewer instabilities compared to an abrupt change of the direction of the flow. These two properties of the boundary layer, namely the thickness and the transition to a turbulent flow will be important in defining the drag.

Boundary layer separation

Another important aspect for the boundary layer is the boundary layer separation. This happens due to changing pressure in the flow direction over the surface of the body. There are no high-pressure changes across a flat surface so boundary layer separation doesn't happen frequently on flat plates. But with curved surfaces, we do have a change in pressure. This can be seen on figure 2.4. At the front of the surface, we have a stagnation point. Here the incoming free-stream flow stops in front of the surface. According to Bernoulli, the static pressure rises if the velocity decreases. So, we have a high-pressure in front of the surface. The flow then goes around the curve and because it has to accelerate to get around the curve, the pressure drops. After the cylinder, the flow gets back to its free stream value where the pressure rises again because the fluid slows down again. So, the fluid goes from high-pressure at the beginning to lower pressure in the middle and then to a higher pressure again at the back.
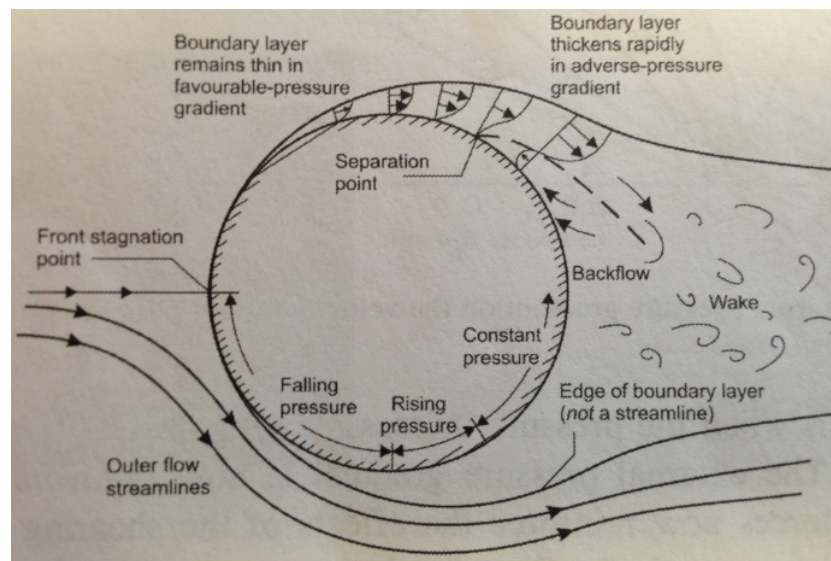
Figure 2.4: Boundary layer separation, [11]

From the front to the middle, there is a favourable pressure gradient ($\frac{dP}{dx} < 0$). The fluid goes from high to low pressure and will accelerate. From the middle to the back there is an unfavourable pressure gradient. The fluid goes from low to high pressure, this is called an adverse pressure gradient ($\frac{dP}{dx} > 0$). Together with skin friction, this unfavourable pressure gradient will slow down the fluid. When this adverse pressure gradient is high enough, the fluid will stagnate and separate from the surface, this point is called the separation point. When separations occur, there is a flow coming from behind the cylinder to the middle, which is called backflow. This will cause a recirculation zone behind the object, called a wake. This wake causes a low-pressure zone behind the object [5]. Streamlining an object can lower the pressure drag drastically, so this low-pressure zone is important for the drag of the car (2.2.6). This streamlining and lowering the pressure drag increases the skin friction drag but the overall drag will decrease. In most cases, the pressure drag is dominant over the skin friction drag.

2.2.3 Vortex shedding

Theory

Vortex shedding takes place when a flow, air in our case, passes a bluff (non-streamlined) body, like a cylinder or a wheel. The boundary layers at each side of the body will detach in a fluctuating manner, causing a fluctuating low-pressure zone behind the body. The oscillation period and amplitude are dependent on the size and shape of the object and on the flow conditions. The low-pressure zone will be bigger than that of a steady one due to this phenomena. There is a certain speed at which vortex shedding starts (called the onset point). With a bluff body (like a cylinder) this onset point is at a very low flow speed (around Re=46) [12, 13]. The repeating pattern created by swirling vortices is called a Von Kármán vortex street. [14, 15]. On figure 2.5 an example of vortex shedding can be seen.
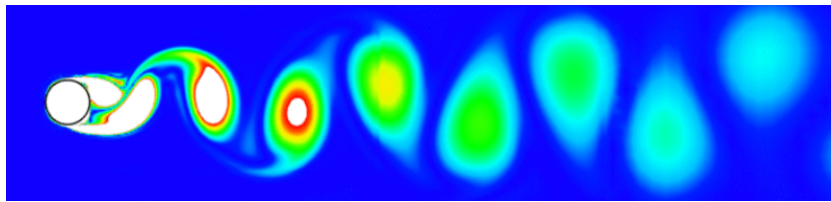
Figure 2.5: Vortex shedding behind cylinder: vorticity

Strouhal Number

The Strouhal number is used to describe vortex shedding. For cylinders, this number has been well studied. One could use these results to check the results of further experiments if one would use a cylinder in similar flow conditions. The Strouhal number is calculated according to formula 2.7

$$St = \frac{f \cdot L}{U} \tag{2.7}$$

where:

St	:	Strouhal number	
f	:	frequency of vortex shedding	[Hz]
U	:	free stream velocity	[m/s]

2.2.4 Turbulence

Turbulence will be an important topic of this research. The flow around the wheel and in the wheel arch will have a lot of turbulent effects. Therefore, it is important to understand the effects of turbulence, the problems in modelling it and how to tackle these problems. Turbulence is present in almost every flow (except micro-flows, extremely slow flows or very viscous fluids). It will create eddies which will get smaller in time because of viscous friction energy loss.

The real origin of turbulence is not yet fully understood but it is assumed that turbulence arises from small instabilities present in the flow. When the kinetic energy is stronger than the dampening effect of the viscosity of the fluid these instabilities will start to grow and become turbulent [5]. If the velocity rises (more inertia), there will be more turbulence. If the viscosity rises (higher viscous forces), there will be less turbulence. This ratio is called the Reynolds number:

$$Re = \frac{\rho \cdot L \cdot u}{\mu} \tag{2.8}$$

where:

Re	:	Reynolds number	
L	:	characteristic length of object	[m]

One can remark that the higher the characteristic length of the object, the higher the chance of turbulence. Below a certain threshold of the Reynolds number, the flow is assumed to be laminar. Above another threshold, the flow is assumed to be fully turbulent. Between these thresholds, the flow is in a transition from laminar to turbulent where both effects occur.

In the view of Kolmogorov [16], there are three main scales in the energy cascade of turbulent flow: integral, inertial and Kolmogorov (seen on figure 2.6). The interaction among the eddies of various scales passes energy sequentially from the larger eddies to the smaller ones: from integral scale to Kolmogorov scale [17]. The Kolmogorov microscales are the smallest scales in turbulence where the eddies dissipate their energy through viscous shear stresses and disappear [18]. Having an idea of these length scales can play a role in defining the resolution of the mesh.
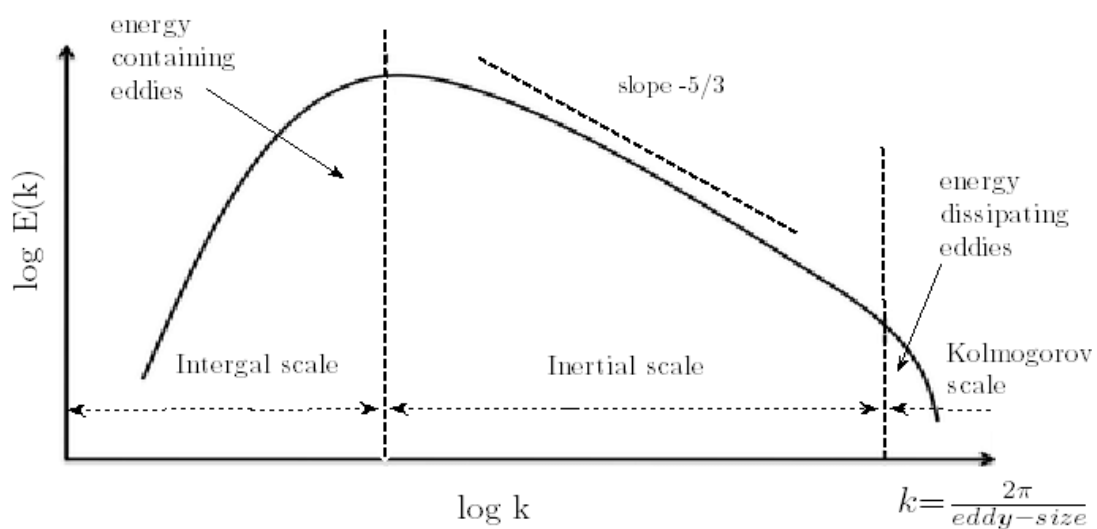
Figure 2.6: Energy cascade in turbulent flows, [19]

2.2.5 Turbulence modelling

Turbulence is a very complex, high frequency and small scale phenomenon. Therefore, it is most of the time not possible to fully simulate turbulence using the Navier-Stokes equations. Instead, turbulence modelling is introduced. The modelling will introduce extra errors and it is therefore again very important to make a compromise on accuracy against computational time.

Summary of models
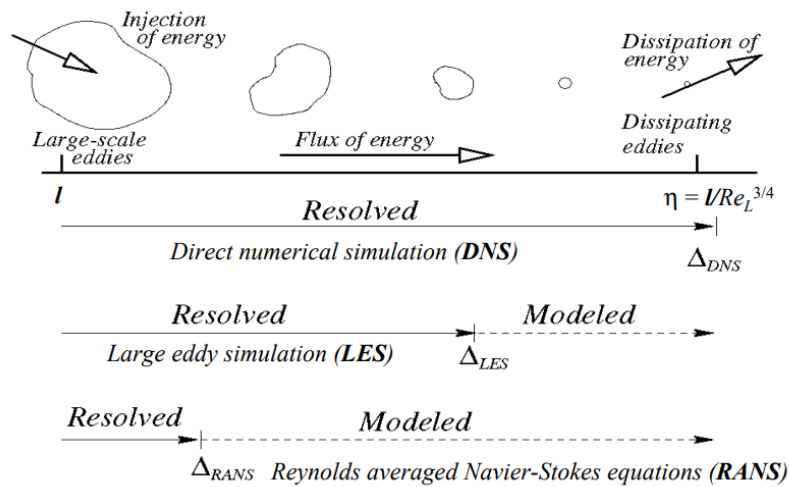
Figure 2.7: Illustration of different models, [20]

The main difference between the methods (RANS, LES and DNS) is how much of the simulation they solve using Navier-Stokes and how much they have to model relying on empirical equations. With modelling the computational effort is lower, but more errors are introduced. On Figure 2.7 you can see an illustration of this for the different models [21]. Except for these three methods (DNS, LES, RANS), there are some methods which are an intermediate solution between two models. The most prominent methods will be discussed.

1. DNS (direct numerical simulation):
   The Navier-Stokes equations are numerically solved without a turbulence model. All scales (time and spatial) are directly, numerically calculated. This needs a tremendous amount of computational power because the power is proportional to the number of nodes, the length of the time steps and the Reynolds number (Re^3). Because the smallest turbulence effects will be solved, a very fine mesh is needed which results in a lot of nodes. The unsteadiness of turbulence requires a very small time step. All these factors make the solving time too long. Especially combined with high Reynolds numbers. DNS is now used for very specific applications and research. An example use is to confirm other models.

2. LES (large eddy simulation):
   This model is time-dependent, it doesn't take the average of the Navier-Stokes equations like RANS. The model makes use of spatial filtering. The eddies (vortices) are calculated from the big ones to the smaller and at a predefined size they are cut off and the smaller eddies aren't calculated but modelled by a sub-grid model. This is, like DNS, more accurate than the RANS models but for complex situations the computational time is too long for now.

3. DES (detached eddy simulation):
   This model combines the best of RANS and LES. In the near-wall regions, the RANS models are used and the rest of the flow is solved with LES. This gives a faster result that

is more accurate than RANS but less accurate than LES.

4. RANS (Reynold's averaged Navier-Stokes):
   Of all methods, RANS models the most, which makes it the fastest model but least accurate.

For our research, we will use RANS models because the more accurate models will need too much computational power and time because of the highly unsteady and complex flow around the wheels. RANS will be described in detail below.

RANS: averaging

Currently, in engineering applications, the most frequently used method is called averaging. The mean flow (statistical) is calculated instead of all the little instabilities that happen in a turbulent flow (seen on the right side of figure 2.8). This kind of simulation yields a result that shows the mean flow, considering the influence of the smaller scale phenomena (which are modelled). This is most of the time sufficiently accurate from an engineering point-of-view. The method for this averaging is called the Reynolds decomposition in which the flow (u) is defined as a mean flow (U) with a fluctuating part superposed on it (u') as can be seen on figure 2.8. The mean flow is derived by averaging the Navier-Stokes equations, losing the time-dependent components. By averaging the equations new unknowns arise because the fluctuating part is neglected. These unknowns are needed to model the effect of the small fluctuations on the mean flow. This is called the closure problem. Extra equations are needed to close the newly formed equations. A clarifying example is shown on figure 2.8. On the figure, a boundary layer is shown in which the velocity at one point is described as a mean velocity which is averaged over a small time interval and has a fluctuating part on top of it.
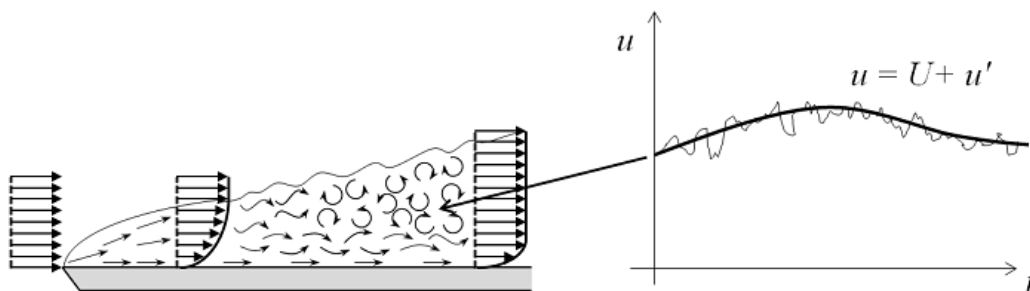
Figure 2.8: Averaging of RANS models in boundary layer and in time, [9]

If we would determine the shear stresses in the fluid based on the mean flow, according to Newton, one would use the following formula: $\tau = \mu \cdot \frac{dU}{dy}$. This is incorrect because there are also fluctuating components in this velocity profile due to turbulent effects. They cause extra shear stresses in the fluid because of the extra movement of the fluid. This example shows that averaging the flow gives rise to new unknowns, namely the effect of the small fluctuations on the

mean flow. The extra unknown that arises in the RANS equations is called the Reynolds stress. This stress resembles the extra stress coming from the fluctuations (u') on top of the mean flow stress (U). The Reynolds stress is equal to: $\tau_{Reynolds} = \rho\overline{u_i' u_j'}$ [22]. The fluctuating component u' is not calculated in RANS, therefore the Reynolds stresses are modelled. The foundation of the models is the Boussinesq approximation which states that the stresses due to the fluctuations can be modelled by adding an extra viscosity, called the eddy viscosity or turbulent viscosity. The turbulence models calculate the eddy viscosity based on other parameters of the flow. Some examples of RANS turbulence models :

1. Spalart-Allmaras: This is a linear one-equation model, this means it solves one turbulent transport equation to solve the closure problem. The variable in this equation is the turbulent kinetic energy k which can be found using empirically determined equations. The Spalart-Allmaras model is robust and fast but lacks accuracy for complex flows.

2. k-ε: This is a linear two-equation model. The variables are the turbulent kinetic energy k and the turbulent dissipation ε. This model is good for free stream simulation.

3. k-ω: This is again a linear two-equation model in which the variables are the turbulent kinetic energy k and the specific turbulent dissipation speed ω. This model is good for simulations near a wall. There is a model, called the k-ω SST variant, which is a combination of the k-ε and k-ω model. It uses the k-ω model in the inner parts of the boundary layer, which makes it suitable to model all the way down through the viscous sublayer to the wall. It gradually switches to the k-ε model for the free stream flow. By gradually switching, it combines the advantages of both models.

4. Reynolds stress model: This model doesn't make use of the isotropic eddy viscosity assumption but instead it calculates the Reynolds stresses directly from six extra transport equations. This is the most accurate RANS-model but also the most computationally intensive one.

A very important remark about the RANS-method is that only the mean flow is visualised. Thus, it is not able to visualise the instantaneous flow field.

Simulation near-wall

A wall has a big influence on the flow, like the formation of a boundary layer. At the wall, high velocity gradients exist which need a very fine mesh. Again, like the simulation of turbulence, a compromise has to be made between accuracy and computational speed. There are different models available to simulate the flow near a wall. In general, you have two types of models:

1. Low Re-number models:
   These models simulate the flow all the way from the free-stream to the surface of the wall. They are used when the interest is on the boundary layer and the conditions at the wall. They are called low Re-number models because the interest is on the viscous sublayer and

the buffer layer. Here the Reynolds number is small relative to the upper turbulent layer. The models need a very fine mesh at the wall because the gradients are very high. That is why it takes more computational power.

2. High Re-number models:

When the Reynolds number is high, the two underlying layers of the boundary layer become very thin. Therefore, they would need a very fine mesh and this causes a very long solving time. That's why these models make use of wall functions. These are again empirically found functions to model the behaviour at the wall and are less accurate. Due to this, a coarser grid can be used, which results in lowering the solving time. These models are used when the interest is in the influence of the wall further away from the wall and not close to the surface.

As seen in section 2.2.2 the y+ value defines the different layers of the boundary layer. Using this value, one can define the properties of the mesh at the boundary layer. The first grid cell of high-Re models has to be between $30 < y+ < 300$. For low-Re models, the first cell has to be at $y^+ \leq 1$, which is in the viscous sublayer [9]. One doesn't want the y^+ be laying in the buffer layer $(1 < y^+ < 30)$ because than it is not possible to use any of earlier mentioned techniques (there are other techniques available like scalable wall functions, which can model till a y^+ value of 11 [23]).

2.2.6 Drag

This section will be about the different types of drag and ways to improve an object to experience lower drag. There are two types of drag relevant for this research, skin friction and pressure drag. The boundary layer will be a very important concept defining the different types of drag and for improving the drag. [24, 25]

Skin friction drag

Skin friction drag is due to the formation of a boundary layer (no-slip condition). Due to the boundary layer, there will be a velocity gradient between the object and the flow around it. The combination of this velocity gradient and the viscosity will cause shear stresses ($\tau = \mu \frac{du}{dy}$) opposed to the direction of movement. This will result in drag. The total skin friction drag is the surface integral of the shear stresses along the surface of the object:

$$\vec{F}_{Shear} = \int_A \vec{\tau} \cdot dA \tag{2.9}$$

The skin friction drag can be best pictured being the drag induced by a flow over a horizontal flat plate [5] as can be seen on figure 2.9.
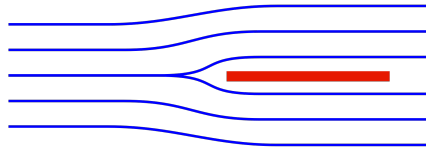
Figure 2.9: Horizontal flat plate in a flow, [26]

The skin friction drag is dependent on different factors. The first factor is the velocity of the free stream flow. If the velocity increases, the velocity gradient will rise and thus the drag force will become higher. Skin friction drag is proportional to u^2 [27]. Also, a higher velocity will encourage turbulence. Turbulence is the second factor which skin friction drag is related to. A turbulent boundary layer will have a higher velocity gradient and thus increases drag. As we have seen in section 2.2.2, turbulence can be avoided by lowering the instabilities. These instabilities may arise from the roughness, the velocity, the shape of the object, etc. A last important factor is the area of the object. The total skin friction drag is the integral of all shear stresses along the surface. Increasing the surface will cause a higher drag. Skin friction drag is proportional to the surface. Thus, if the skin friction drag has to be lowered, one has to lower the speed, prevent instabilities and lower the surface area. [28] [29] [30]

Pressure drag

The pressure drag is also related to the boundary layer. As can be seen in section 2.2.2, the boundary layer can separate from the surface. This will result in a high-pressure at the front because of the stagnation of the fluid and a lower pressure at the back because of the wake (seen on figure 2.4), creating a net force or drag. The total pressure drag is the surface integral of the pressure along the surface of the object:

$$\vec{F}_{pressure} = \int_A \vec{p} \cdot dA \qquad (2.10)$$

The pressure drag can be best pictured being the drag induced by a flow at a flat plate perpendicular to the flow [5] as can be seen on figure 2.10.
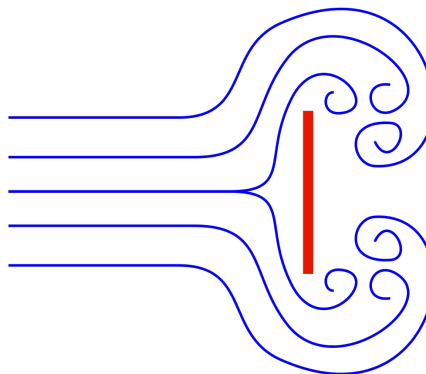
Figure 2.10: Perpendicular flat plate in a flow, [26]

To lower the pressure drag one can do two things. The first one is to lower the pressure at the front. This can be done by lowering the frontal area or to change the geometry in such a way that the flow will go smoothly around it. The second way is to reduce the size of the wake at the back of the object to reduce the low-pressure area. If the boundary layer separates very early on the object, the wake will be big. Thus the size of the wake can be reduced by pushing the separation point further to the back. This can be done in several ways. One way is to change the geometry of the object to ensure the flow leaves the object in a smooth way. This will alter the adverse pressure gradient. Another way is to create a turbulent boundary layer by for example using vortex generators. A turbulent boundary layer contains more kinetic energy and will come to a stop further to the back. The method of changing the geometry to create a better pressure profile around the object is called streamlining. An example of a good shape is a water droplet with the point facing backwards [28], this is because of the late separation point (seen on figure 2.11).

Figure 2.11: Streamlined body in flow, [31]

Relation between skin friction and pressure drag

In optimising skin friction and pressure drag one can see there is a relationship between the two. Some factors may optimise both, some factors will optimise one and make the other worse. For example, to optimise pressure drag we may want to make the object longer so that the flow can leave the object in a smooth way to reduce the wake. This will add surface to the object and thus increase the skin friction drag. Another example is turbulent flow. Turbulent flow will cause more skin friction drag but will lower the pressure drag. So according to the shape of the object and the conditions of the flow, one has to find an optimum in optimising the drag. When the shape of the object approximates a horizontal flat plate, skin friction will be dominant, thus the focus will be on optimising the skin friction. Pressure drag will be dominant when the shape approximates a vertical flat plate or a highly curved shape. For this type, one might want to encourage a turbulent flow. An example of this are dimples on a golf ball. In certain conditions, one type of drag may be dominant. For our case, the skin friction drag will be dominant for the car itself because it is a very flat, streamlined profile. For the wheels themselves, the pressure drag will be dominant.

Interference drag

There is also another type of drag that may be relevant for us, which is the interference drag. Interference drag is present because the car is not a single body but is an assembly of different structures. The combination of different bodies always has a greater drag than the sum of its parts. This is because the flow characteristics on every object are different and the interference of these flows will increase the total drag.

General formulation of drag

The previously described types of drag can be written into one equation to get the resulting drag
force:

$$F = \frac{1}{2} \cdot \rho \cdot u^2 \cdot C_d \cdot A \tag{2.11}$$

where:

A	:	surface area	$[m^2]$
C_d	:	the drag coefficient	

The surface area is normally taken as the area of the object perpendicular to the flow. C_d is a
coefficient which contains the effects of pressure and skin friction drag. Because of the changing
effects with changing velocity of these two types of drag, C_d is not a constant. It is in function of
the Reynolds number [5]. For cars, this value is taken constant because of the small Reynolds
number interval of driving velocities. Another way of describing the aerodynamic performance
of a car is the C_dA value, which is the multiplication of C_d and A. This value is a good indicator
because it includes C_d, which says something about how good the shape of the car is and also
includes A, the actual frontal area of the car.

2.3   Beat

Beat will be discussed in the results of this research, therefore the theory behind it will be de-
scribed in this section. Beat is the phenomenon that takes place when two signals with a (slight)
difference in frequency are superposed. This is shown on figure 2.12.
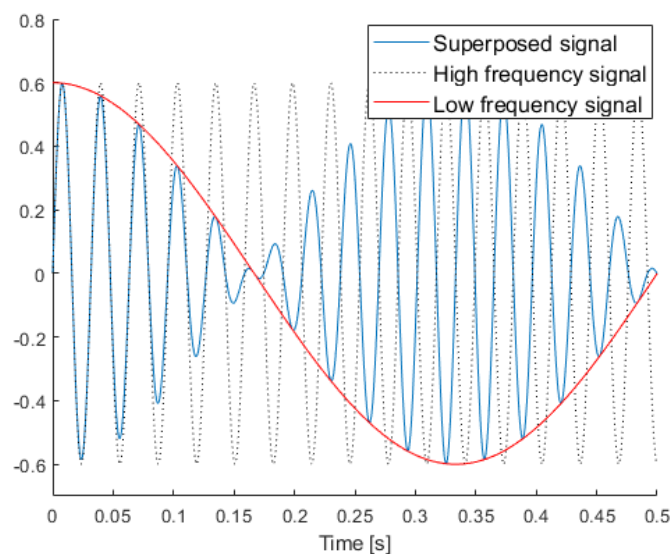
Figure 2.12: Example of beat

Because of the slight difference in frequency, there is constructive interference at one point and destructive at another. This causes two noticeable frequencies in the system: one lower enveloping frequency and one higher frequency. These frequencies can be calculated with the following equations:

$$f_{low} = \frac{f_1 - f_2}{2} \tag{2.12}$$

$$f_{high} = \frac{f_1 + f_2}{2} \tag{2.13}$$

with:

- f_1 and f_2 the original frequencies of the signals that are superposed

- f_1 the highest frequency of the two

Chapter 3

Literature study

Present knowledge and previous researches about aspects of this research will be discussed. With this knowledge, the most appropriate methods can be selected specifically for the case in this research.

Wheels are a major contributor to the aerodynamic drag of land vehicles. The flow around these wheels is very complex due to the many separation regions created by very small tyre features and by the contact area of the tyre with the ground. In the past, they tried to mimic the flow around the wheels by isolating the effect of rims and isolating the effect of the tyres but there has been shown that there is an interaction between these two which makes it necessary to investigate them simultaneously. Many of the previous studies have been dedicated to the understanding of the significance of tyre geometry on the drag of vehicles. But these studies are numerically particularly challenging since proper computation of the rotational condition is difficult due to the many complex and small tyre features, the area at contact with the ground, the deformation of tyres because of a certain load, etc.. [32]. The important aspects about the modelling of rotating wheels which will be discussed are: rotational condition, turbulence model and expected results.

3.1   Rotational condition

There are different available methods to model the rotation of wheels, each with their specific advantages and disadvantages:

- **Sliding Mesh**, looks numerically the best solution to correctly model the rotation. It allows adjacent meshes to slide relative to one another, which means that the mesh of the wheel will rotate in time according to its speed. Sliding mesh has to be an unsteady simulation [33] because the rotation is done by rotating a part of the mesh itself. For a time-accurate solution of the rotating wheel (rather than a time-averaged solution) this method is desired. This study will not use sliding mesh because it focuses on the time-averaged solution and the contact patch (seen in 4.6) is difficult to implement in a sliding mesh. Sliding mesh is used in the study of Hobeika et al. [32] to check the accuracy of a newly developed hybrid

method (MRFg), which will be discussed later.

- **Moving wall boundary condition (MW)** is the most common method. It introduces a velocity term at the wall which is tangential to the cell surface. So the wheel itself will not rotate but a thin layer of fluid at the surface of the wheel will be given a velocity to mimic rotation. This has one major drawback: due to the conservation of mass, the velocity cannot have a component normal to the cell surface as this would be physically interpreted as in/outflow through a solid wall. On figure 3.1 this can be seen for the indicated zone. A wheel that is modeled by a moving wall boundary condition is shown on the left, a wheel modeled by a sliding mesh is shown on the right. On the right, a velocity will be present at the indicated area because of the rotation of the mesh itself. On the left, with a moving wall boundary layer, this velocity can not be applied because it is normal to the surface. Because of the geometrical complexity of normal rims and tyres many surfaces would not be modelled correctly with this method as their movement is in a direction normal to the surface [34]. One should note that this research is not about a normal rim/tyre but about the solar car tyres, which doesn't have rims (see figure 3.2). This minimises the disadvantage of the Moving wall boundary condition.

(a) Rotating wall   (b) Sliding Mesh
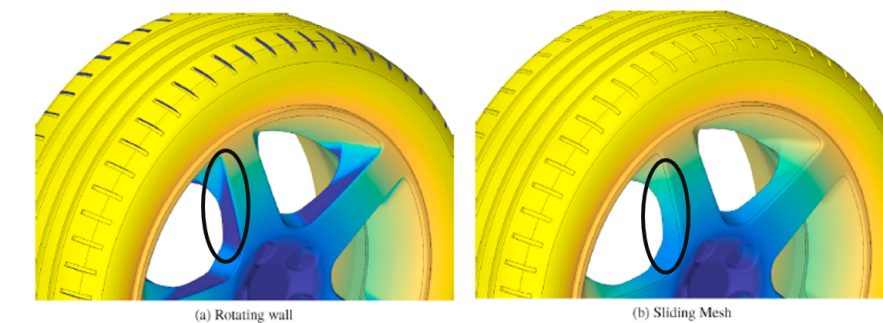
Figure 3.1: Modelling of rotation for a normal rim/tyre, velocity, [32]

- **Moving reference frame (MRF)**, is the last alternative discussed to model the rotation of the wheel. It introduces a separate computational domain adjacent to the wheel rim where the flow is solved using the rotating reference frame equations. [35]. The moving reference frame can overcome the problem of MW by setting the fluid as part of a local rotating reference frame with respect to the global reference. This introduces centrifugal accelerations and Coriolis effects into the fluid. MRF is not desirable to do with a flow perpendicular on the axis of rotation, because of the used equations it will induce a strong pressure gradient which could alter the velocity by more than 40% [32]. A hybrid method developed by Hobeika et al. [32] is Moving Reference Frame -grooves (MRFg), which combines the best of both MRF and moving wall boundary.

From the research of Lescniewicz [35] and Hobeika et al. [32], it can be concluded that use of Multiple Reference Frame (more specifically MRFg) decisively helps to obtain a numerical model with higher accuracy with respect to their experiment. Even though the higher accuracy, this

research will still use a moving wall boundary condition. The main disadvantage of this method: not being able to model the flow normal to a wall, isn't important for the solar car wheels because they lack spokes and so lack these kinds of walls (as seen on figure 3.2). This method is both faster and still suitable for comparing a rotating to a stationary wheel.

The contact patch will be modelled by immersing the tyre through the computational domain.
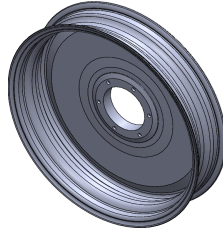
Figure 3.2: CAD drawing of solar car rim

Besides the selection of the used rotational condition, it is important to choose which turbulence model will be chosen and to check with other researches what the expected results would be.

3.2 Turbulence model

The thesis of Uten and Vandervelpen [1] has been devoted to the acquisition of a mesh of sublime quality and the search for an appropriate turbulence model for the Punch Two solar car. The research has investigated the differences between 5 different turbulence models.

1. Spalart-Allmaras

2. k-ω SST

3. k-ε

4. RSM

5. Transition g Re q SST

The best choice to model the aerodynamic performance of the Punch Two solar car, if computational time and accuracy are compromised, is the k-ω SST model. This is especially valid during early design stages because the team would be able to adjust quickly because of the fast computation times. During the late design phase, the research suggests using the SST transition model, which is reasonably able to forecast the transitioning of the boundary layer. Our results can be compared to a certain extent to the results of Uten and Vandervelpen if we choose any of these 5 turbulence models. Even though both researches will examine the same car, it is not possible to draw clear conclusions from this comparison because their research hasn't included the wheels in their simulations (nor stationary or rotating). But still the results of our research should be relatively close to their results and according to [34] the drag is lower for rotating wheels than for

stationary wheels.

From this research, other researches [36, 37, 38] and a small research discussed later on, it can be concluded that k-ω SST is the best choice for modelling the flow in this research.

3.3   Expected results

The research "Aerodynamics of a rotating wheel in a wheelhouse" of Viswanathan V. [39], studies the aerodynamics of a rotating wheel in a wheelhouse, mounted in a simplified body. This simplified body is the body used by Fabijanic [40] in his research and is already well studied. The use of a simplified body makes it possible to keep the cell count low (5.1 million). This low cell count and the high computational power available makes it possible to use LES for the simulations which is much more accurate than RANS. The methods used in this research are not suitable for our research because of the different solving technique, but the results can be used to check our results.

The research of Waschle [41] focuses partly on the difference observed in the flow field, between a stationary wheel or a rotating wheel with a stationary or moving ground. The first case representing the wind tunnel environment, the second case representing the real-world condition. The research found that the rotation of wheels had two main effects:

1. The rotation produced a narrower wake behind the wheels, improving the underbody flow of the production car.

2. This narrower wake led to a smaller separation bubble at the rear of the car, which leads to a smaller low-pressure zone and a reduced drag force because of this.

These researches and their results can be used to check the results of our research till a certain extent. All the previous mentioned researches study a wheel inside a wheelhouse of a production car. The distance between wheel and the wheelhouse is much bigger than the distance between wheel and wheel arch of the Punch Two.

Chapter 4

Mesh generation

The mesh generation is very important for this research. The mesh has to be of sufficient quality to yield good results, but because of limited computational power, it is important to keep in mind the higher computational power needed for an increasing number of cells. In this chapter important factors of the mesh are described. All numbers used in this chapter are of the converged mesh which is used in the end results. The previous research of Emmerick and Joachim [1] was about the creation of a good mesh for the solar car. Their experience will be used for generating the mesh and adapt it to the car with the wheels. To generate the mesh, OMNIS$^{\text{TM}}$ is used, which is software from NUMECA.

4.1 Geometry and simplifications

The first step in the mesh generation is the geometry itself, generated in CAD-software. The geometry was provided by the Solar Team and then adapted to make it suitable for the mesh generation. In the following two sections the geometry of the car and the wheels is described.

4.1.1 Car

The geometry of the car is from the Punch Two, the same one that has been used in the previous thesis [1]. On figure 4.1, the outside geometry of the car is shown.
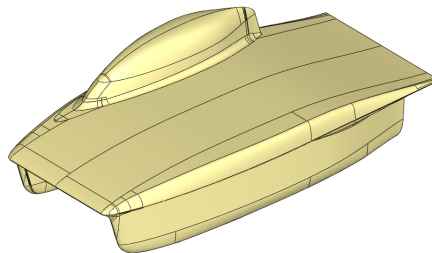
Figure 4.1: Geometry of the car

In this geometry, the wheels are added because they were neglected in the previous thesis [1]. The wheel placement is according to the geometries of the real car which has a track width of 1220mm and a wheelbase of 1550 mm. Figure 4.2 shows the wheel positions.

(a) Bottom of the car   (b) Section view front left wheel
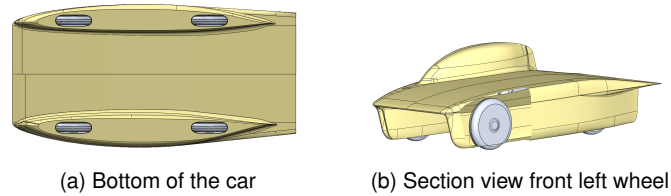
Figure 4.2: Placement of the wheels

4.1.2   Wheel and wheel arch

The wheels consist out of 3 parts: the rim, the tyre and the wheel arch. This assembly is shown in a section view on figure 4.3.

(a) Front view   (b) Back view
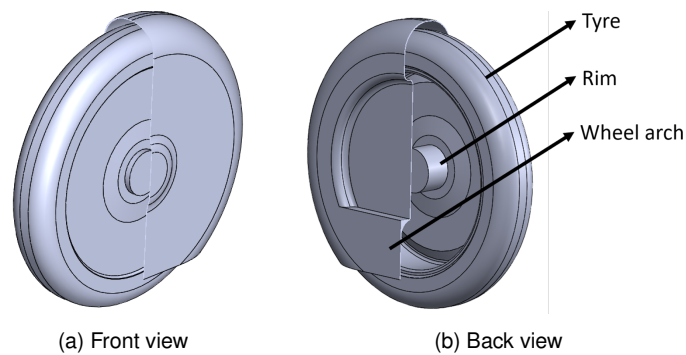
Figure 4.3: Assembly wheel section view

Again, reasoned simplifications have been made to reduce the computational time. First, the rim has been simplified. The curves on the inside were removed as well as small holes for the bolts. Normally the rim is connected to the suspension. This has been replaced by one single axle. The real and simplified rim are displayed next to each other on figure 4.4.

(a) Real rim   (b) Simplified rim
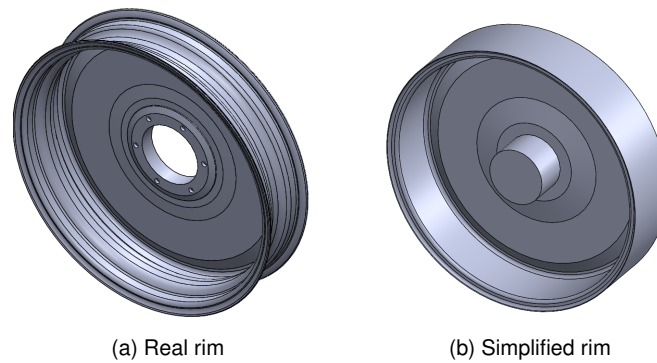
Figure 4.4: Comparison real and simplified rim

For **the tyre**, the grooves were removed. This is because it mainly consists out of circumferential grooves (see figure 4.5) which will not alter the flow that much when rotating. The design of the grooves and the impact on the flow can be a subject of further research.
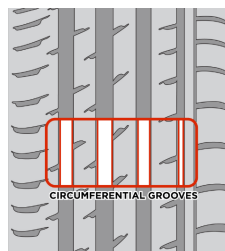
Figure 4.5: Example of circumferential grooves, [42]

Remark: the lines that seem to appear on the tyre on figure 4.3 indicate that the wheel has a flat surface, not that it has grooves.

The wheel arch also had some minor changes. First, the gap for the suspension was closed because the flow inside the car is neglected. Also, the indent at the side (see figure 4.6) is simplified. On figure 4.6, the section view of the real and the simplified arch can be seen.

(a) Real arch   (b) Simplified arch
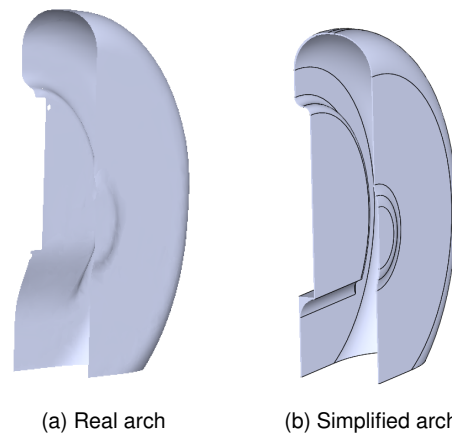
Figure 4.6: Comparison real and simplified arch

To reduce the computational time the car is sealed so that no flow can enter the car and no mesh is needed internally. This simplification is justified because the main focus is the effect of the wheels on the outer flow. The sealing has been done by closing the gap between the shell of the car and the wheel arch (see figure 4.7). Because of this sealing, there is only flow possible between the wheel and the wheel arch and not inside the car.

(a) Real car with gap   (b) Simplified car: no gap between wheel arch and car
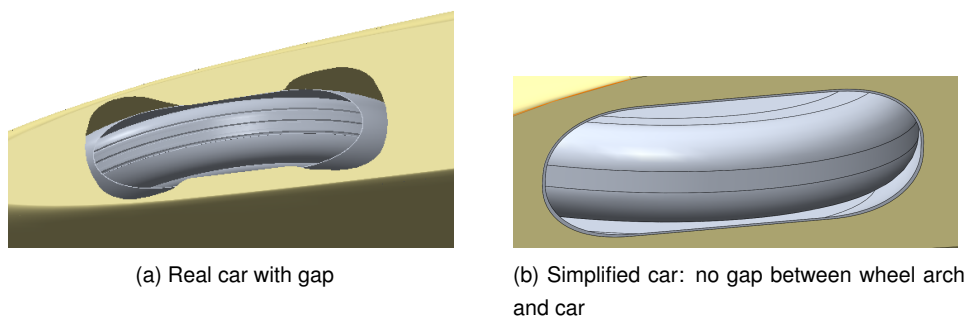
Figure 4.7: Comparison real and simplified car

4.2 Symmetry

As seen in figure 4.1 the car is not fully symmetrical. Nevertheless, only half of the car will be meshed. This is to maintain the cell count to a minimum. Although the car is not fully symmetrical, the goal of the research is to find the influence of the rotating wheels on the drag of the car and not to find the exact amount of drag. Therefore, using only half of the car is justified because there will be more time available to do other analysis and also to have a more detailed mesh in certain parts, like for instance around the wheels. For this research, the half of the car without the canopy will be used as can be seen on figure 4.8.
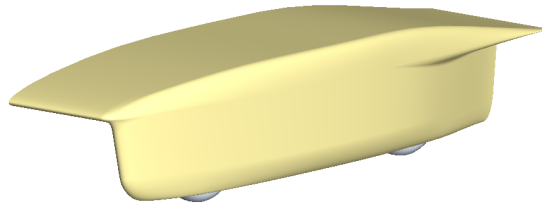
Figure 4.8: Half of car used in simulations

4.3 Domain
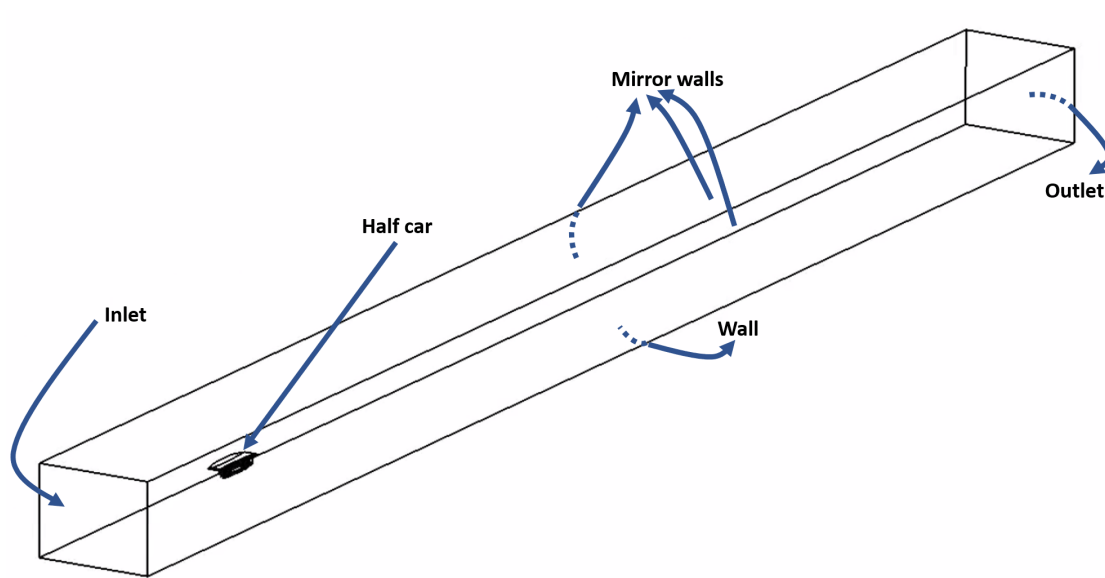
Figure 4.9: Computational domain

The domain size has to be big enough that the boundaries have no influence on the flow around the car but also keeping the cell count minimal. The size of our domain is based on research done in the past to obtain the optimal domain size for a solar car [4]. The outcome of this research shows that a domain of 25L x 7W x 5H is sufficient, the car must be placed 5L away from the inlet. The rough dimensions of the half car are 3238 x 789 x 912mm so the domain dimensions are 81 x 5.7 x 4.6m. The domain size is validated in chapter 6 to check if the boundaries have no influence as expected.

The cell size in the domain, initially, is also based on previous researches and best practices in which is stated that in the far field there should be 10-15 cells in the smallest dimension of the domain [4]. This leads to a domain cell size of 0.45m, which will be the biggest cell in the grid and will be refined closer to the car.

The boundaries (seen on figure 4.9) of the domain need a type according to their function. For the sides and the top of the domain, a mirror type is chosen. This way they have the least effect on the flow because they resemble the 'infinite' world around the car. One side mirror plane will act as a symmetry plane because the simulation is only for half of the car. The bottom of the domain is taken as a solid wall. This is necessary because the ground needs to be able to generate viscous forces. Otherwise, the flow will not be physical. There will also be an inlet and outlet boundary. The flow conditions at these boundaries will be explained in chapter 5.

The cell geometry is chosen dependent on the geometry of the object. If possible, a hexahedron only grid is used. This is because it yields less cells which makes it faster to solve. But if the geometry of the object is too complex a hybrid grid (combination of tetrahedron and hexahedron cells) is preferred as a hexahedron only grid will not be able to capture the geometry properly. Although the car has a rather complex shape, a hexahedron only grid is still able to capture the geometry. Both type of grids have been made for the current setup, a hybrid grid needs 17 million cells and a hexahedron dominant only needs 11 million for the current setup. On figure 4.10, the final hexahedron dominant grid is shown.

(a) Leading edge of car

(b) Wheel
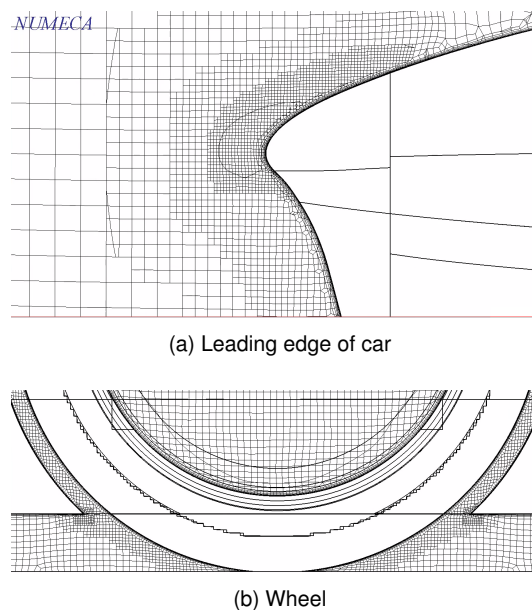
Figure 4.10: Capturing of hexahedron dominant grid

4.4 Refinements

The cell size of the domain has to be refined around the car to be able to capture the geometry and high-velocity gradients. First, the car will have a general refinement. One could choose to make this general refinement small enough that it captures all the details of the car. But this will result in a very high cell count. Therefore, the general refinement will be chosen in such a way that it's sufficient enough for the simple, big elements of the car. The car will then be further divided

into parts which will get a further refinement based on their geometry and velocity gradients. This section will describe the refinements of important surfaces/edges as well as refinement volumes and their purposes.

4.4.1   Edges of the car

Although this research is mainly focused on the wheels, the car itself also needs to be captured in a good way. This is because of the interaction of the flow between the car and the wheels. This part will be based on previous research [1] because the geometry of the car is the same as used in their research. Also, because the drag of the car with the wheels will be compared to the car without the wheels, it is very important to have the same reference. Thus, a similar mesh for the car itself is created. Some changes are made to reduce the cell count in comparison to the previous research because the wheels still have to be added in this research and it's important to keep CPU-time as low as possible. In figure 4.11 the important edges and surfaces of the car are indicated. Only the edges on one half of the car are mentioned because the research will focus on this part of the car.
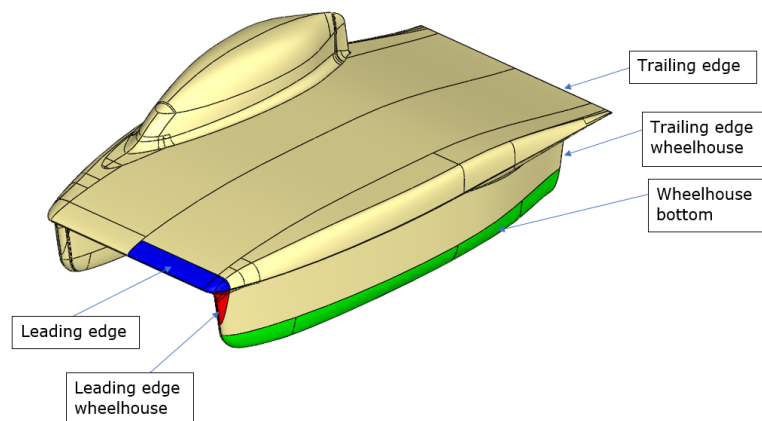
Figure 4.11: Important edges of the car

The leading edge

It is very important to capture the leading edge in a good way because it is the first contact with the free stream flow. The stagnation point and high-velocity gradients require a fine mesh. Therefore, extra refinements and curve divisions are added. On figure 4.12, the capturing of the leading edge can be seen.

Figure 4.12: Leading edge capturing

The trailing edge

Past researches [1] [43] have shown that it is very important to capture the trailing edge in a way that it forms a smooth edge at the end of the car. That is why it received extra attention. On figure 4.13 the capturing of the trailing edge can be seen.
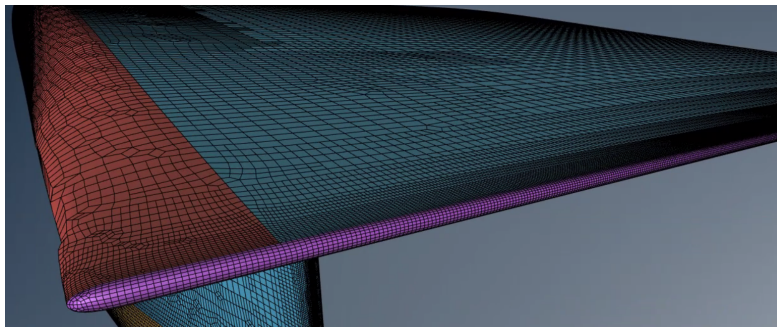
Figure 4.13: Trailing edge capturing

The wheelhouse edges

The wheelhouse is very defining for the flow that will reach the wheels. Like the upper foil, it also has a leading and trailing edge. On figure 4.14, the capturing of the wheelhouse can be seen.

(a) Leading edge wheelhouse   (b) Trailing edge wheelhouse
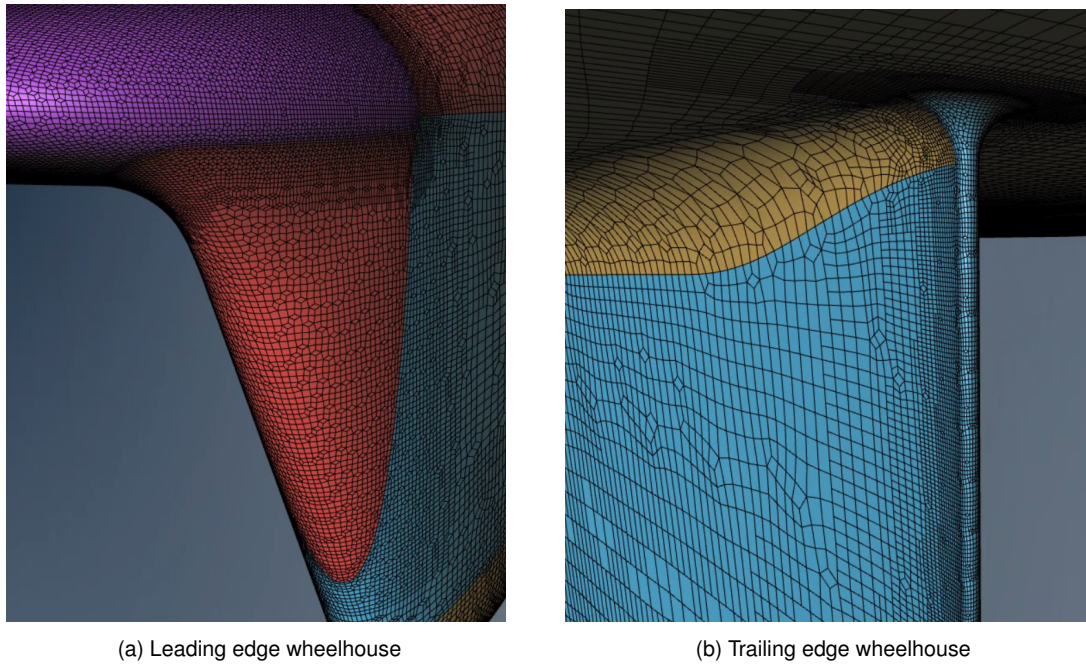
Figure 4.14: Wheelhouse Capturing

Also, the bottom part of the wheelhouse is refined to capture the gradients caused by the wheels.

4.4.2   Wheels

The wheels are the main focus in this research; therefore it is very important that they are captured in a good way. The most important parts are the curves of the arch and the curves of the tyre. Also, extra attention is needed for some of the edges. Important edges are the indent of the arch, the bottom of the arch and the edge between the tyre and the rim. On figure 4.15, the meshes of the wheel and arch are shown.

(a) Mesh of arch

(b) Mesh of wheel
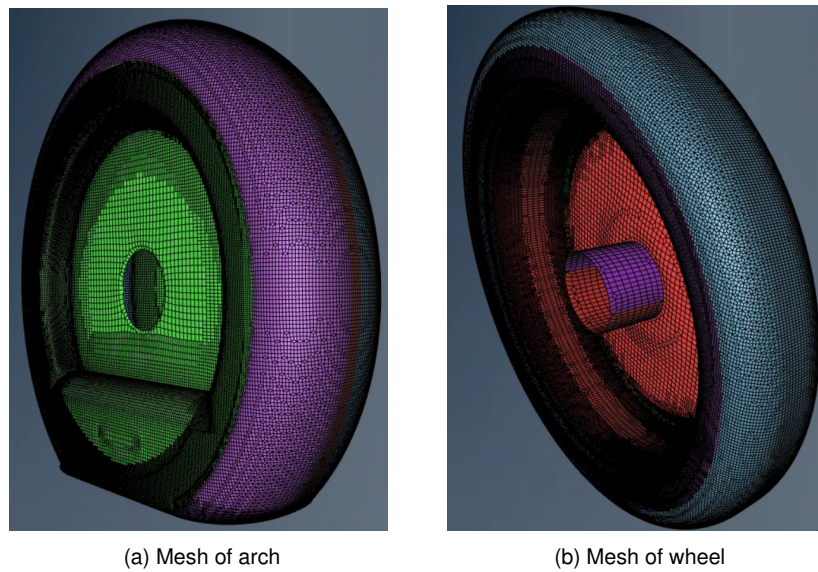
Figure 4.15: Capturing of the wheel

As can be seen, the curves are captured by the mesh and the edges have a higher refinement. Remark that the hole in the arch is closed because the axle of the wheel will merge into it.

Another important refinement is between the wheel and the arch. The space between them is small relative to the car, there are high-velocity gradients and the flow between the arch and the wheel is of high interest. For this refinement, a proximity refinement is used. With this feature, the cell size is based on how close the two are to each other. Because this distance is variable, this feature will result in fewer cells compared to a fixed refinement. On figure 4.16, a section view of the wheel is shown with some dimensions to have an idea of the size.
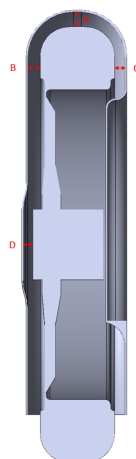
Figure 4.16: Section view of wheel

On figure 4.17, the proximity mesh is shown. As can be seen, the cell size changes when the two

A	B	C	D
19.28mm	15.24mm	13.53mm	12.17mm

Table 4.1 Dimensions spacing wheel and wheel arch

get closer to each other.

(a) Section of wheel

(b) Close-up on proximity

(c) Close-up on proximity from side
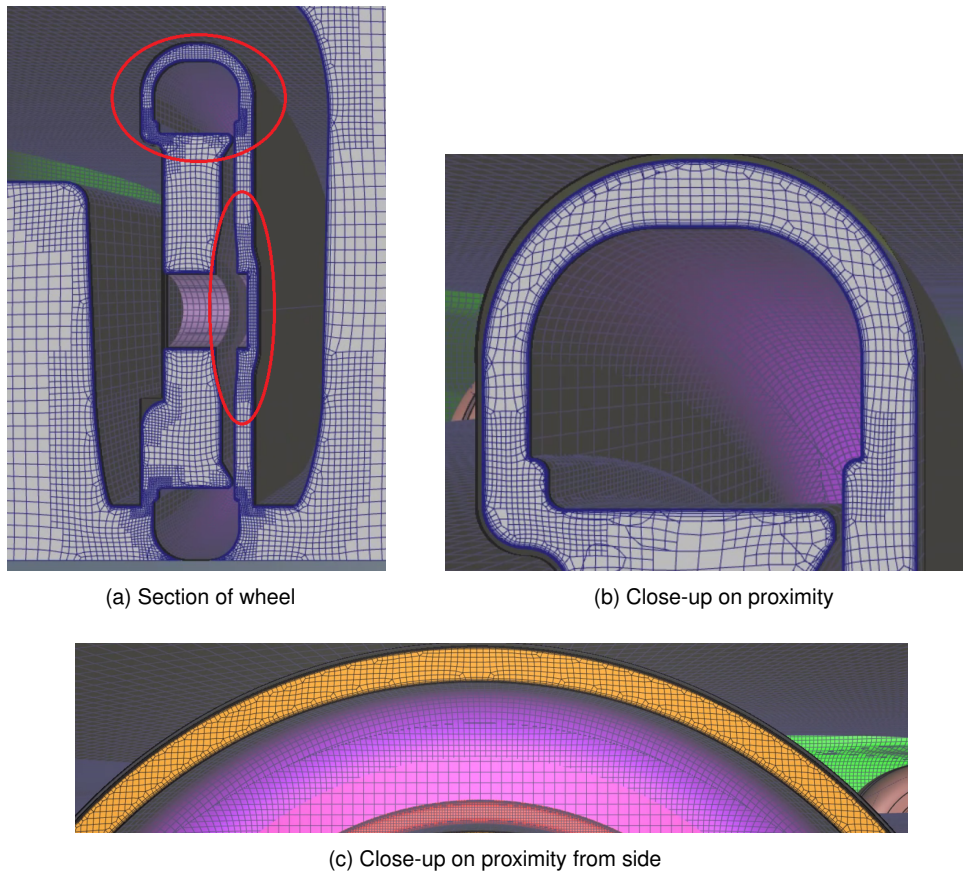
Figure 4.17: Proximity refinements between wheel and wheelarch

4.4.3   Refinement volumes

In the previous part, the refinements of surfaces was described. Next to that, refinement volumes are added. In our research, three volumes were added with each a specific goal (seen on figure 4.18). First, a cubic volume was created around the car. The function of this volume is to capture the gradients very close to the car. Next to that, a bigger box is added that has twice the length of the car. This box is needed to capture the wake behind the car. This second box has bigger cells than the one around the car. Around the wheels, a cylindrical volume was added. Again, this is needed to have a finer volume to capture the gradients inside and around the wheels.
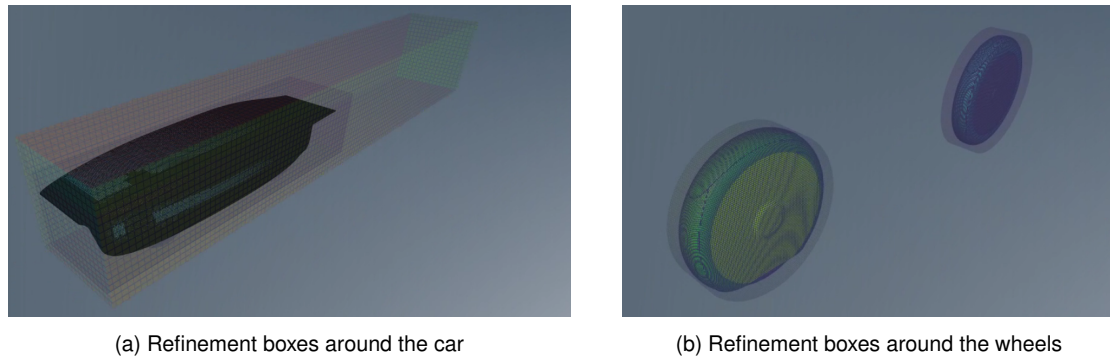
(a) Refinement boxes around the car

(b) Refinement boxes around the wheels

Figure 4.18: Refinement boxes in the domain

4.5 Viscous layers

The near-wall treatment of a surface can be done in two ways: Low-Reynolds-number modelling or high-Reynolds number modelling, both ways have been briefly discussed in 2.2.5. The first method implies that the boundary layer will be resolved numerically, the second method implies that the boundary layer is not resolved, but approximations are introduced to account for the flow behaviour across it [44]. For the low-Reynolds modelling, viscous layers are added in the mesh. This is done on relevant surfaces, where the boundary effects are important. This is the case for all parts of the shell. Here the skin friction due to shear stresses must be accurately calculated. Also, the wheels need viscous layers to capture the points of separation accurately.

The first layer thickness y_{wall} should reach a $y^+ \leq 1$ which can be used inside the Blasius equation, to approximate a value as the initial value (see 4.1). After the research one should check that indeed $y^+ \leq 1$, because the Blasius equation is only valid for a flat plate. The stretching ratio is kept on the standard value of 1.2, which means that the cell size will increase by 20% for every extra layer.

$$y_{wall} = 6 \cdot \left(\frac{U}{v}\right)^{\frac{-7}{8}} \cdot \left(\frac{L_{ref}}{2}\right)^{\frac{1}{8}} \cdot y^+ \tag{4.1}$$

where:

y_{wall} :   first layer thickness $[m]$

For the wheel, the value of y_{wall} should be 17.97 μm. To calculate the number of viscous layers needed, equation 4.2 is used. This equation is based on the stretching ratio, calculating the number of layers needed to stretch from first layer thickness to the size of the surrounding cells.

$$SCS = y_{wall} \cdot (SR)^n \tag{4.2}$$

where:

n :   number of viscous layers

SR   :   Stretching ratio = 1.2

SCS   :   surrounding cell size   [m]

The surrounding cell size is 14,0625mm with the current mesh settings, this is the biggest cell near the wheel. According to this equation, 37 viscous layers would be needed by the biggest cell. In proximity of the smaller cells between wheel arch and wheel, there would be 22 viscous layers needed. Because of the small size of viscous layers, the total number of cells rapidly increases if there are many viscous layers. Therefore, the number is limited to save on computational power. Limiting the number of viscous cells is done in several ways:

- No viscous layers are added on the floor because the floor is a flat plane and moves at the same speed as the free stream flow (driving conditions). Therefore, there will be no boundary layer on most part of the floor. For the area around the car the boundary layer will be modelled with wall functions, if a boundary layer is present.

- Limiting the viscous cells can be done by limiting the number of layers added on an object. This means the cell size will not stretch fully to the size of the surrounding cells. If the expansion ratio is too big, errors will be introduced. Therefore, a compromise must be made. In the case of the wheels, 10 layers are used instead of the theoretical 37. This compromise results in an expansion ratio between 18.0 and 126.4. This expansion ratio is too big and would introduce major errors, but one should note that this expansion ratio is a worst-case scenario in which the high-velocity gradients are adjacent to the big cell sizes and where there is no diffusion of cell size applied. The eventual maximum expansion ratio will be checked after the creation of the mesh (see 4.7.2).

- Adjusting the parameters of the viscous layers to the local velocity lowers the amount of viscous cells. The flow between the wheel arch and the wheel itself will probably have a smaller velocity than the free stream flow (certainly for the stationary wheel). The y_{wall} would be bigger for this slower flow (if y^{+} remains 1), which eventually would result in a lower number of viscous layers for this part. This method is not used because of the high complexity in the software to have different viscous layers on one part, as well as the high number of iterations needed to get this method correct.

On figure 4.19, the stretching of the viscous layers of the mesh between the wheel and the arch can be seen.
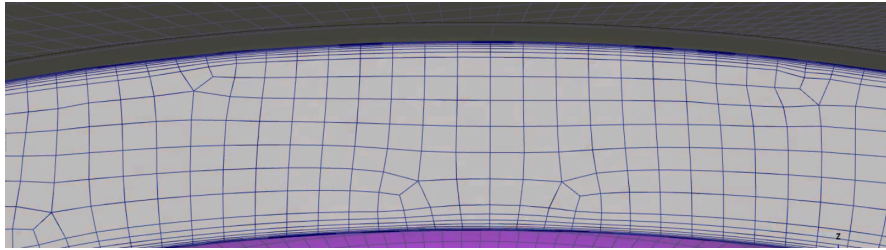
Figure 4.19: Viscous layers wheel

In chapter 6.2 the values of y^+ at the surfaces will be validated.

4.6 Contact patch

The part of the tyre which is in contact with the ground, is called a contact patch (see figure 4.20). The contact patch is responsible for the traction of the car with the ground. In the simulations, the contact patch is being represented by submerging the car and with this the tyres through the computational domain. The side bulge of the tyre will be neglected, so the shape of the tyre will remain intact.

Figure 4.20: Contact patch tyre, [45]

The selected tyre of the Punch Two is Bridgestone K1650 95/80R16 RA01AZ Tubeless Radial. The cruising speed of the solar car is around 25m/s and the total weight is around 213kg (driver of 70kg included). Unless one will perform a practical test for determining the contact patch, it is nearly impossible to calculate this exactly. Therefore, approximated models based on practical tests are used. The data of the tyre has been used to calculate the contact patch according to the method of an online calculator: 'Tire Data Calculator' [46], which bases the calculations on The Automotive Chassis: Engineering Principles 2nd ed [47] and practical tests. The resulting contact patch is 67mm width and 29mm in length. From this data, one can calculate the total submersion in the domain needed to generate this contact patch, which results in a submersion of 0.38mm. On figure 4.21, the contact patch of the mesh can be seen (yellow).
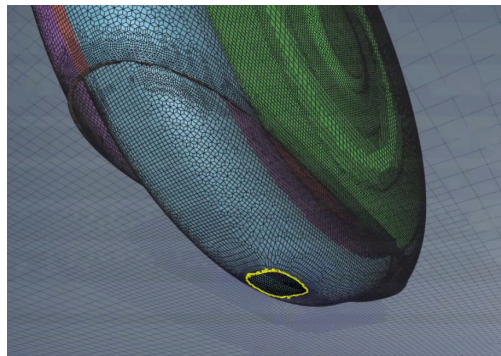
Figure 4.21: Contact patch mesh

4.7 Mesh quality

Before using the mesh in the solver, the quality has to be checked. In this section, certain factors of the mesh will be evaluated. It has to be noted that the mesh generation is an iterative process, meaning the mesh that will be checked for quality is the final used mesh (mesh 3,normal). Before this quality check, a convergence study was done as shown in section 6.1.1, leading to this final mesh.

4.7.1 Skewness

The maximum skewness is an important factor for mesh quality. It shows how good (or bad) a cell is approaching an equilateral cell. It is important that the cells approach an equilateral cell because the equations used in the solver are based on equilateral cells. A quality mesh would have a maximum skewness of 0.4 in a 3D simulation (with 0 being a perfect mesh with all equilateral cells) [48]. The maximum skewness will be checked for the final mesh (mesh 3, normal). This results in figure 4.22. Even though there are a lot of cells with a higher skewness than 0.4, the mesh is still sufficient. Most of the high skewness cells are situated at the bottom of the wheels, where the wheel is submerging in the domain. This part of the domain is a difficult section to mesh.
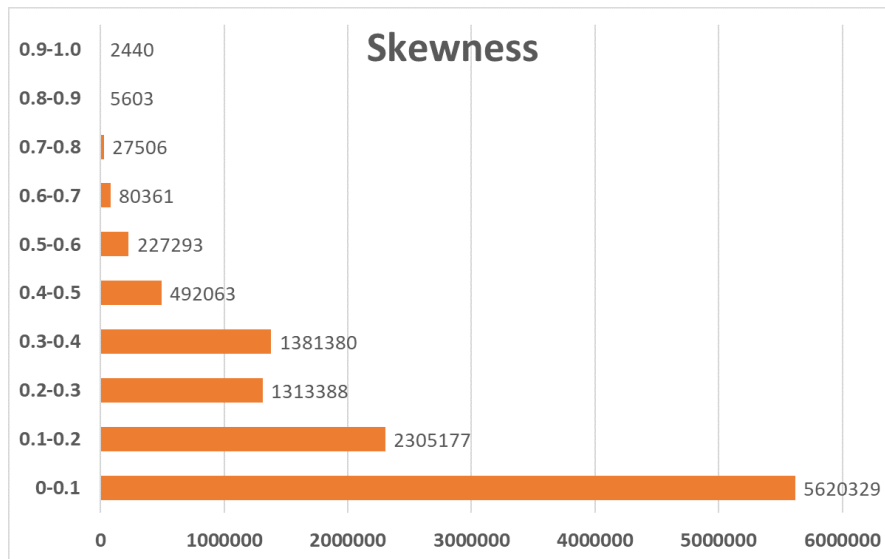
Figure 4.22: Skewness of mesh 3

4.7.2 Expansion ratio

The expansion ratio is another important factor which will be looked at in this mesh quality analysis, as this is also stated in section 2.2.5. The expansion ratio is a measure of the size variation between two adjacent cells. The distribution of these cells is visible on figure 4.23. All cells are well within the acceptable range of 20 for the expansion ratio [49].
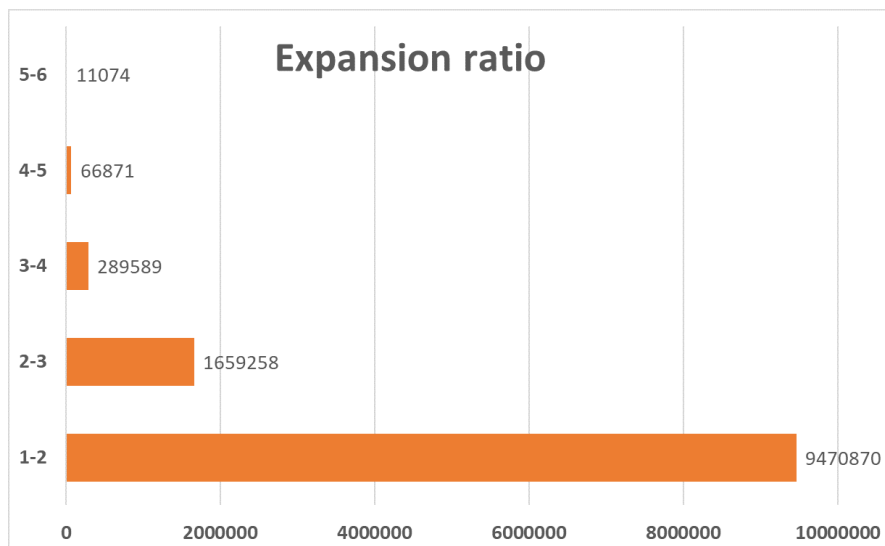
Figure 4.23: Expansion ratio of mesh 3

4.7.3   Twisted, negative, concave cells

A last important check in the mesh quality analysis is the check for 'bad cells' (twisted, negative or concave cells). There should be none of these cells present in the mesh.

Twisted cells are cells with a distorted shape. In these cells, a vector is wrongly oriented [50].

Negative cells are cells with a negative volume. This can happen if a face orientation is wrongly oriented which lead to a negative volume if the volume is vectorial calculated [50].

Concave cells are cells where the Jacobian of the transformation to a unit cube has at least one zero value for a point located within a cell.

Conclusion

The mesh doesn't have any of the three mentioned bad cells. No further research into these type of cells is necessary.

Chapter 5

Solver settings

The next step, after the creation of the mesh, is to use this mesh in a flow solver. First of all, a small research is conducted to select the proper turbulence model. After that, the solver specific parameters are defined. The solver used in this research is Fine^{TM}/Open solver 8.1, provided by NUMECA. At the end, the computational power setup is described.

5.1 Selection of turbulence model

In chapter 2.2.5, the theory behind some turbulence models has been briefly discussed as well as the reason why a model is needed. According to the research of Vandervelpen and Uten [1] the k-ω SST captures the flow of the Punch Two solar car the best while keeping CPU-time reasonable. For the wheel itself, a small research was conducted with a free stream across a cylinder (representing the wheel), both stationary as rotating. The rotating simulation didn't have vortex shedding, the stationary wheel did have these vortex shedding. The vortex shedding is used to check the results with the theory by calculating the Strouhal number (see 2.2.3) of the flow behind the cylinder. Performing a Fourier transform on the results from the simulation gives a frequency spike around 211Hz, which is called the frequency of the vortex shedding. This frequency results, according to formula 2.7, in a Strouhal number of 0.212, which is close to the theoretical value of 0.21 at a Reynolds number of 5800 according to figure 5.1. This small research confirms that the k-ω SST model is sufficient to model the flow around the wheels. The k-ω SST model is sufficient for both the solar car 3.2 as well as the wheels so it can be concluded that it will be sufficient for the combination of them.
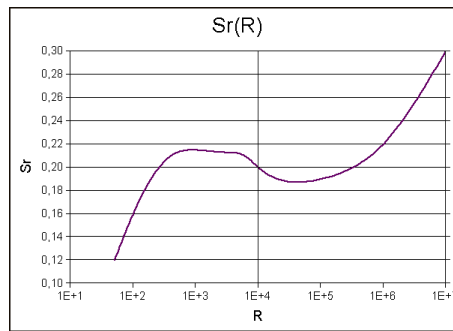
Figure 5.1: Strouhal number and Reynolds number, [51]

5.2 Solver parameters

In this section the solver parameters for the Fine^{TM}/Open solver 8.1 are defined.

5.2.1 Parameters of turbulence model

The k-ω SST model combines both the k-ω and the k-ε model. The resulting model uses the k-ω model near solid walls and the standard k-ε model, in a k-ω formulation, in the free stream [52]. Both the turbulent kinetic energy (k) and the turbulence dissipation rate (ε) need to be calculated for this model. According to formula 5.2 the turbulence intensity (T_u) is needed.

The inlet is being numerically represented by a boundary condition on the inlet wall which dictates that the flow will have a speed of 25m/s in the direction of the car at this wall. The turbulence intensity of this wall needs to be calculated in order to know k and ε at this boundary. Because all simulations are being checked by the wind tunnel results, it is important to mimic the wind tunnel conditions as closely as possible. The solar car is being placed at 5m from the inlet in the wind tunnel from Ford in Cologne. In the simulations, this distance is 16.3m. The turbulence intensity in the wind tunnel at the inlet is 0.18%. This turbulence intensity quickly decays so at the computational inlet this value has to be higher to reach the same value at 5m in front of the car, which can be calculated according to formula 5.1. From this formula follows that the turbulence intensity at the computational inlet is 0.38%. With the turbulence intensity known, is it possible to calculate k and ε. According to equation 5.2, the value of k is 0.0138 m^2/s^2. The value of ε is 1.168 m^2/s^3 according to formula 5.3.

To reduce the possibility of oscillations in skin friction due to non-physical relaminarization during convergence, it is recommended by NUMECA [4] to set the value of $\varepsilon_{initial}$ to 10% of ε.

$$T_u = \sqrt{T_{u,inlet}^2 \cdot \left[(1 + \frac{3 \cdot \rho \cdot U \cdot x_{inlet} \cdot \beta \cdot T_{u,inlet}^2}{2 \cdot \mu \cdot (\mu_t/\mu)} \right]^{\frac{-\beta^*}{\beta}}} \tag{5.1}$$

$$k = \frac{3}{2} \cdot (U \cdot T_u)^2 \tag{5.2}$$

$$\varepsilon = C_\mu \cdot (\frac{\mu}{\mu_T})(\frac{\rho \cdot k^2}{\mu}) \tag{5.3}$$

where:

T_u	:	turbulence intensity at inlet computational domain	[%]
$T_{u,inlet}$	:	turbulence intensity at inlet wind tunnel	[%]
x_{inlet}	:	streamwise distance between inlet wind tunnel and computational domain	[m]
μ_t/μ	:	turbulence viscosity ratio	[/]
β	:	0.09 (constant)	
β^*	:	0.0828 (constant)	
k	:	turbulence kinetic energy	[m^2/s^2]
ε	:	rate of dissipation of turbulence energy	[m^2/s^3]
C_μ	:	0.09 (constant)	

5.2.2 Boundary conditions

Inlet wall: as stated in section 5.2.1, the inlet condition is defined as a subsonic flow of 25m/s in the direction of the car. The turbulence model parameters are being defined according to the calculations made in section 5.2.1.

Outlet wall: is being represented as a static pressure imposed boundary condition. This static pressure is equal to atmospheric pressure. It is important to check, after the calculations, that there are no abrupt changes in the pressure plot close to the wall, as this can indicate that the domain is too small.

Top and side walls: these walls should all be mirror walls which is achieved by selecting Euler wall. This means that there will be no velocity profiles on these walls. This way they have the least amount of influence because they represent the 'infinite' world behind the car. Also, one side plane acts as a symmetry plane for half of the car.

Floor: the floor is being represented by a wall. This means that there will be velocity profiles with corresponding boundary layers formed on this wall (these boundary layers are modelled with a high Re-number model). For the velocity boundary condition of the floor, there are two options. The first one is to use a stationary floor as this mimics a stationary car in the wind tunnel. A second option is a moving floor as this mimics a driving car. For this research, it is chosen to use a moving floor because the flow field created by the rotating wheels in driving conditions is the focus of this research. One could argue that in the comparison of the stationary and rotating wheels, the stationary wheels could be simulated with a stationary floor and the rotating wheels with a moving floor. This, however means that the rotation of the wheels changes as well as the boundary conditions in the comparison of both scenarios. This makes it harder to draw conclusions for the causes of possible differences. Therefore, it is opted to use the same boundary conditions for both.

Because of the same speed of both floor and the airflow, there will be no boundary layer on the floor as long as the flow isn't disturbed.

Car and wheels: the car is being represented by a wall. The wheels are also wall with an extra boundary condition: the rotation. The rotation is being represented as a Moving Wall Boundary condition, as stated in section 3.1. The rotational velocity is 855.92 RPM, which equals the linear velocity of 25m/s of the car itself.

5.2.3 Unsteady simulation parameters

Because there is no repeatable pattern visible in the steady simulation nor is there a convergence visible in the drag, it is recommended to perform an unsteady simulation for this research. The time step of the unsteady simulation is initially calculated according to the Courant number (see equation 5.4). The Courant number is an indicator for the stability of the simulation, as this indicates the number of cells a fluid particle travels during one time step. After some iterations, to speed up the simulation, the eventual time step is 3.86ms. This time step will be used for all simulations in this research. The time step still leads to more than 20 time steps per period which is recommended by the NUMECA documentation. The actual Courant number is 48.2 for the smallest cells. One should note that this is the worst case scenario in which the smallest cell is present in the highest velocity flow.

$$C = u \cdot \frac{dt}{dx} \tag{5.4}$$

where:

C : Courant number

dt : time step [s]

dx : mesh size [m]

5.2.4 Numerical parameters

Numerical scheme

In the numerical parameters of the Fine^{TM}/Open solver it is possible to change the spatial discretisation. This influences the amount of artificial (numerical) dissipation used to stabilise a solution. Because the flow is unstable (vortex shedding) it is recommended to use a scheme with a less dissipating character [4]. Because of this, the scheme is changed from the default 2nd-order central scheme to 2nd-order central matrix scheme. The use of a 2nd-order scheme implies that the order of convergence used in section 6.1.1 theoretically equals to 2.

5.3 Computational power setup

The computational power that was available for this research was the following:

1. 26 Cores (Intel Xeon Gold 6152)

2. 500GB HDD Drive

3. 160GB RAM

Chapter 6

Results

This chapter describes the results of the research. First of all, the results are verified and validated. This is a very important step because CFD always yields to results but they are not always meaningful. After that, the influence on the drag with rotating wheels will be described as well as the flow around the car.

6.1 Verification

In the verification, the mathematical properties of the results are verified.

6.1.1 Mesh convergence study

To check mesh convergence, certain criteria [53, 54, 55] have been developed to check this in a standardised way. These criteria will be discussed in this chapter. For a mesh convergence study, it is best to have at least three different mesh sizes, which each have at least a difference of 10% in cell count. For convenient reasons, the mesh convergence study will only be done for the scenario with the stationary wheels. There have been 4 mesh sizes modelled, the results from this are shown on figure 6.1. It is clear from the figure that the result from mesh 1 to 3 is similar and that the result from mesh 4 is different (especially amplitude of oscillation). Mesh 4 doesn't capture the vortex shedding well because of the higher numerical dissipation that comes with a coarser mesh. Mesh 1 isn't far enough calculated, due to the computationally intensiveness, to perform a viable analysis. This leads to the selection of mesh 2 and 3 to perform the mesh convergence study. The properties of these meshes are shown in table 6.1.

(a) Mesh 1: ultra-fine mesh drag curve (79 timesteps)

(b) Mesh 2: Fine mesh drag curve (448 timesteps)

(c) Mesh 3: Normal mesh drag curve (654 timesteps)

(d) Mesh 4: Coarse mesh drag curve (74 timesteps)
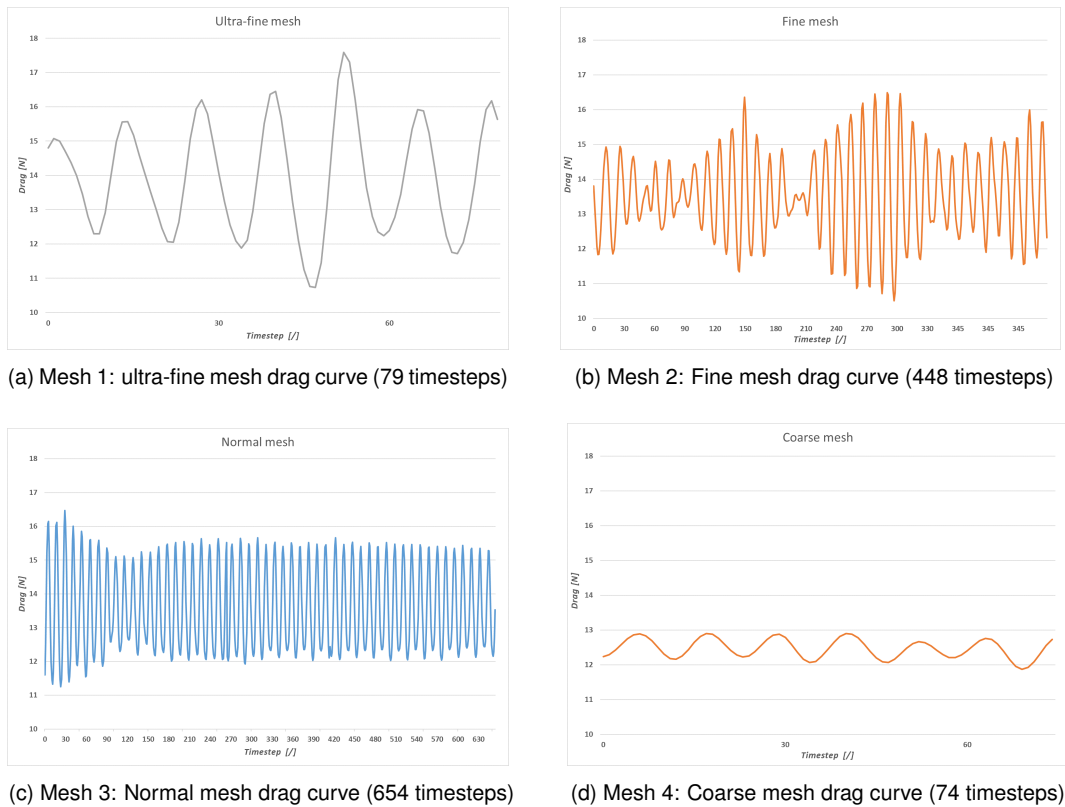
Figure 6.1: All meshes drag curves

Mesh type	Number of cells	Domain cell size [m]	Proximity minimum size [m]
Mesh 1 (ultra-fine)	16806373	0.35	0.002
Mesh 2 (fine)	13727978	0.40	0.002
Mesh 3 (medium)	11500490	0.45	0.002
Mesh 4 (coarse)	8956853	0.9	0.003

Table 6.1 Different mesh parameters

The drag has a fluctuating and changing pattern because of vortex shedding and non-linear behaviour. This leads to three criteria for the mesh convergence: average drag, root-mean-square drag and most present frequency (calculated with Fourier transform). The refinement of the mesh is $r_{23} = 1.194$, which shows that there is more than 10% difference in the mesh cell counts.

The order of convergence, o, is one of the primary ways to estimate the actual rate of convergence, the speed at which the errors go to zero. For the equations used in the turbulence models, this value is theoretically 2. This could only be checked if there are at least 3 different meshes studied, in this study the theoretical value will be used. In table 6.2 the different mesh types are shown with the corresponding results.

Mesh type	Average drag [N]	RMS [N]	Frequency [Hz]
Mesh 2 (Fine)	13.55	13.62	20.62
Mesh 3 (Normal)	13.61	13.67	20.74

Table 6.2 Different mesh types with their results

The fractional deviation in results will be calculated according to formula 6.1

$$\delta_{32} = \frac{s_3 - s_2}{s_2} \tag{6.1}$$

where:

s :   variable for which convergence study is performed   [N or Hz]

δ :   fractional deviation

The grid convergence index (GCI) provides a consistent manner for reporting grid convergence. It is derived from the theory of generalised Richardson Extrapolation [53]. This grid convergence index indicates how much of an error there is still present if the estimated solution would be calculated from the simulated results, according to formula 6.3. This error is quite conservative and the real error will, in almost all cases, be lower.

$$GCI = \frac{F_s \cdot \delta}{r^o - 1} \tag{6.2}$$

where:

F_s :   safety factor = 3

GCI :   Grid Convergence Index   [%]

r :   refinement ratio

o :   order of convergence

$$s_{exact} = s_2 + \frac{s_2 - s_3}{r_{23}^o - 1} \tag{6.3}$$

This results in table 6.3 for the three criteria.

	Average drag [N]	RMS [N]	Frequency [Hz]
Estimated solution	13.41	13.50	20.34
GCI [%]	3.13	2.59	4.11

Table 6.3 Estimated solutions and their GCI for three mesh convergence criteria

This means, that based on the current results, a solution can be estimated if the mesh was infinitely refined. The estimated solution of the final converged average drag would be 13.41 [N] with a variation of 3.13 %. From this, it can be concluded that the mesh is sufficiently converged.

6.1.2 y^+ **Values**

As stated in section 2.2.5, the value of y^+ should preferably be lower than 1 and certainly not higher than 5 to prevent that the first cell would be situated in the buffer layer. On all surfaces, for which the boundary layer is important and modelled by adding viscous layers, the y^+ values are plotted and can be seen on figure 6.2. It is clear that the values rarely get bigger than 1 and are almost always smaller than 2. The part of the tyre inside the arch in the stationary simulation has a very low y^+ value due to the lower velocity. In this simulation, it would have been possible to change the first viscous layer thickness for this area to make the simulation faster. But because there are multiple scenario's which will be compared to each other, it's important to keep the same mesh.

(a) y^+ value of car with stationary wheels

(b) y^+ value of stationary wheels

(c) y^+ value of rotating wheels

(d) Scale of y^+ values
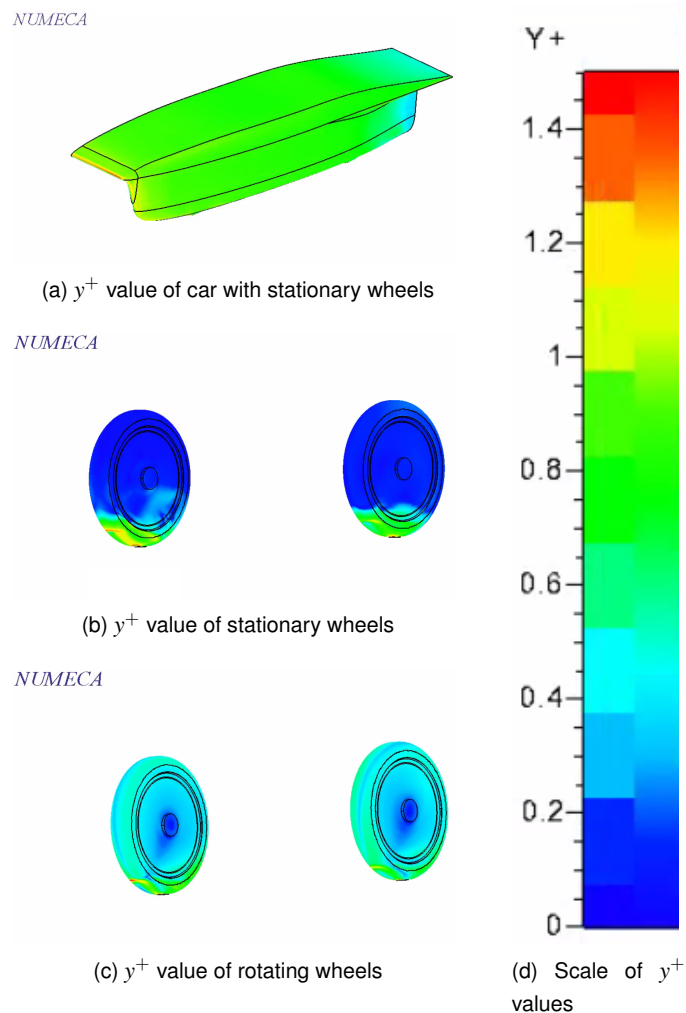
Figure 6.2: y^+ values of car for rotating and of wheels for both simulations

6.2   Validation

After the verification, the results still have to be validated. This means the physical behaviour has to be checked and the results are compared to results of the wind tunnel tests.

6.2.1   Domain size check

As stated in section 4.3, it is important to check that the boundaries indeed have no influence on the flow. This check is done by plotting the pressure throughout the domain. The expected result is that the pressure would be nearly constant close to the wall, the pressure would change in proximity of the car and then get back to a constant value. Because the simulation performed, is a simulation of a half car, only the pressure plot from front-to-back will have this development. Both side-to-side as top-to-bottom will only have one stable value and the other side will be the car. The plots are seen on figure 6.3. From these plots, it is possible to conclude that the domain is big enough to have little to no influence on the flow around the car.
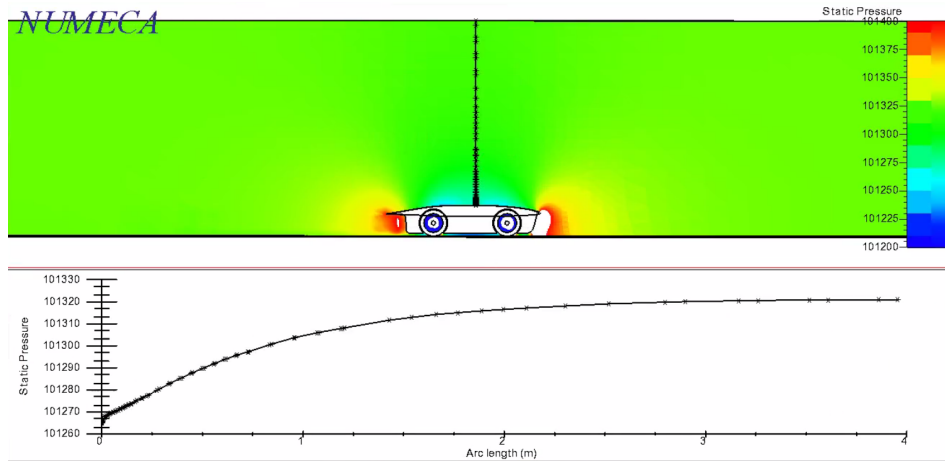
(a) Pressure plot top-to-bottom domain
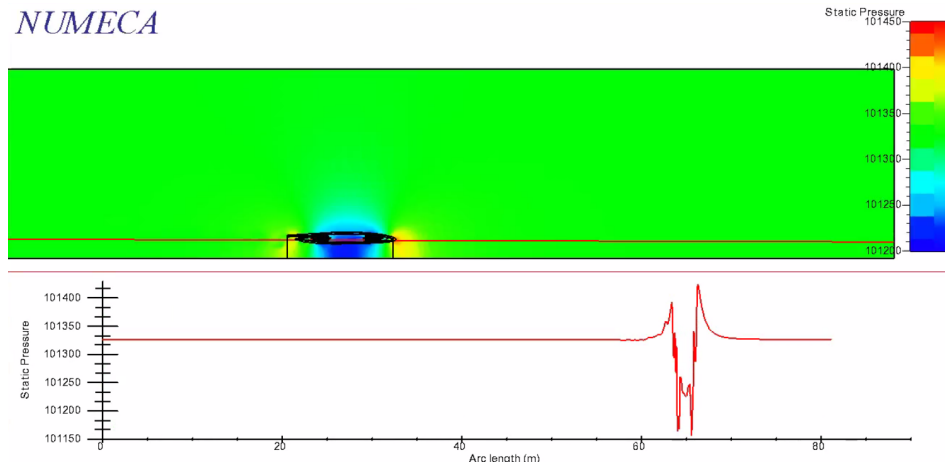
(b) Pressure plot front-to-back domain direction
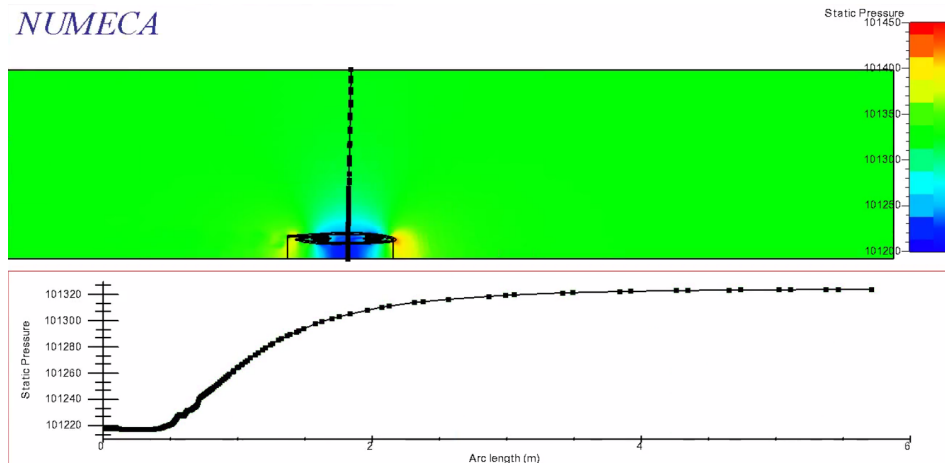
(c) Pressure plot side-to-side domain

Figure 6.3: Pressure plots through the domain

6.2.2 Rotation of the wheels

The rotation of the wheels is a very important parameter in this research. Different methods to mimic rotation are described in section 3. For this research, the 'Moving wall boundary condition' method is used. This is a simple, less accurate method but very time-efficient. Also, because of the closed rim design of the solar car, this should be sufficiently accurate. This is because the major drawback of the 'Moving wall boundary condition' method is the modelling of components normal to the rotation, like a spoked rim. These features are not present for this wheel geometry. In this section the rotational velocity on the wheels is validated. On figure 6.4 the velocity vectors on the full wheel are shown. It can be noticed that the velocity is 0 in the middle and equal to 25 m/s at the outer radius of the wheel. This is a first indicator that the rotation is modeled in a good way because of the constant angular velocity and actual velocity of $v = \omega \cdot r$. Figure 6.5 shows a close-up where the actual vectors can be seen. It is clearly visible that all vectors rotate around the rotational axis of the wheel. It can therefore be concluded that the rotation is validated.
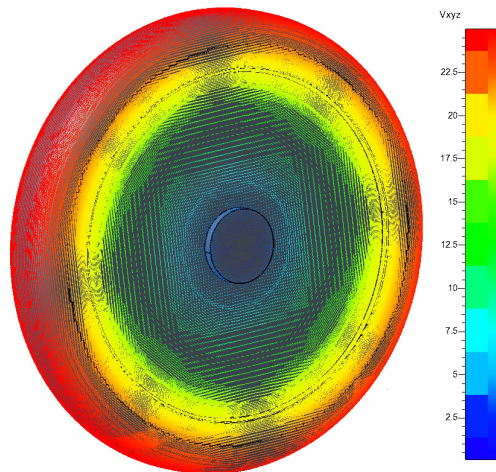
Figure 6.4: Vxyz surface plot of full wheel
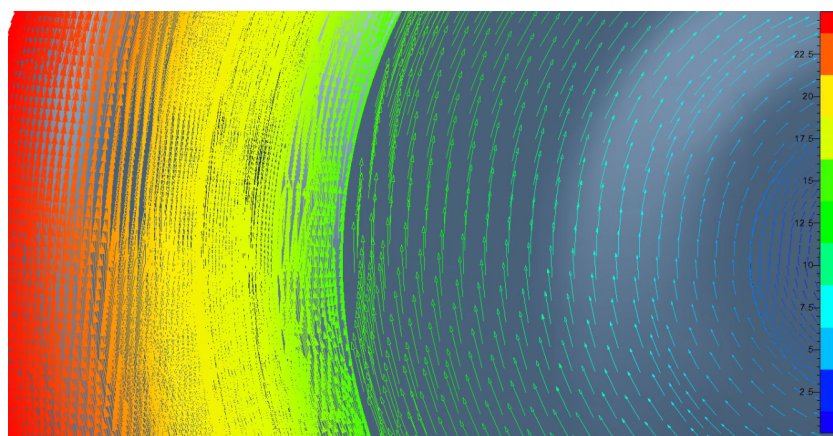
Figure 6.5: Vxyz surface plot close-up, arrow dictates flow direction

6.2.3   Comparison to wind tunnel test results

After the convergence study and the check of the physical behaviour, the results are compared to results coming from the wind tunnel tests done by the Solar Team. The C_dA value coming from the wind tunnel is 0.084. In the wind tunnel, the wheels are stationary, so they are compared with the stationary simulation of this research. To compute the C_dA for the current research, the drag forces of the car have to be extrapolated. This is because of time constraints, only half of the car was simulated. In section 6.4.4 the extrapolation is described extensively. After the extrapolation, the total drag results to 31.84N. The C_dA value is calculated according equation 6.4:

$$C_dA = \frac{2F}{\rho \cdot u^2} = \frac{2 \cdot 31.84}{1.225 \cdot 25^2} = 0.0832 \tag{6.4}$$

The resulting C_dA from the simulation is very close to the C_dA of the wind tunnel tests and shows a deviation of 0.95%.

One should note that the simulation in this research does have a moving floor which is not the case in the wind tunnel. Nevertheless, this was the only data to compare the results to and can give insight if the results are in the right order of magnitude.

6.3   Computational times

A quick overview of the computational times will be given, to have an idea of the time scale. The time periods that are defined can be used by future Solar Teams to predict whether they have enough time to do analysis on the wheels. All time values given are the wall-clock times needed for the simulation on the given computational power setup, discussed in section 5.3. It also shows that, even though a finer mesh yields a better result, the compromise of time and accuracy is very important in CFD-simulations. Mesh 3 (normal) has been simulated till it was stabilised, the other meshes were stopped before this point. Mesh 2 (fine) has been simulated the second furthest to perform the mesh convergence study (seen in section 6.1.1). For mesh 1, time was not sufficient to let it also fully stabilise. The 'time needed to stabilise' in table 6.4 is the estimated time needed for every simulation to reach the same amount of timesteps as mesh 3 needed to stabilise for stationary wheels.

Mesh 3 with rotating wheels was also computed upon stabilisation. An interesting conclusion from this, is that the simulation with rotating wheels needs significantly less time (only 10%) to stabilise in comparison to the simulation with stationary wheels. If the KU Leuven Solar team wants to simulate the car with wheels included, it is best to include the rotation for faster stabilisation.

Mesh type	Steady	Unsteady	Average time per timestep	Time needed to stabilise
Mesh 1 (Ultra-fine)	48h 35m	94h 47m	28m 26s	490h 32m
Mesh 2 (Fine)	78h 12m	124h 56m	26m 15s	452h 49m
Mesh 3 (Normal)	52h 03m	439h 27m	25m 29s	439h 27m
Mesh 4 (Coarse)	36h 56m	22h 12m	13m 44s	236h 49m
Mesh 3 (Normal) *rotating*	47h 44m	44h 18m	21m 37s	/

Table 6.4 Computational times

6.4 Influence of rotation on drag

The main goal of this research is to find the difference in drag between stationary and rotating wheels for the Punch Two solar car. This difference will be used to estimate the real-life drag (rotating wheels) from the results coming from the wind tunnel (stationary wheels). First of all, vortex shedding is described because this phenomenon causes the major difference between the stationary and rotating wheels and most of the other phenomena are consequences of the vortex shedding. Following that, the influence of rotation on the different types of drag, namely skin friction and pressure drag, will be described. At the end of this section, a model for the drag difference will be discussed.

6.4.1 Vortex shedding

The flow behind the stationary wheels shows bigger fluctuations than the rotating wheels. This is due to the formation of vortex shedding. With vortex shedding, the boundary layers at each side of the wheel separate in a periodical way as described in section 2.2.3. This causes the fluctuating pattern behind the wheel as shown on figure 6.6.
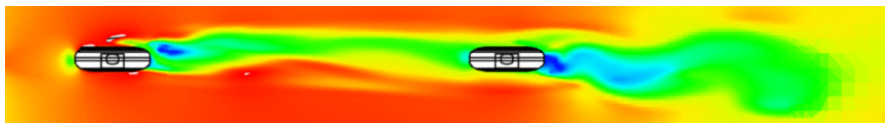
Figure 6.6: Magnitude of V for stationary wheels showing vortex shedding

Vortex shedding is also present at the rotating wheels but due to the rotation, which suppresses vortex shedding [41], this results in smaller fluctuations. On figure 6.6 and 6.7, the magnitude of the velocity for respectively the stationary and rotating wheels at one time step is shown. If figure 6.6 and figure 6.7 are compared, it is clear that vortex shedding is smaller with the rotating wheels.
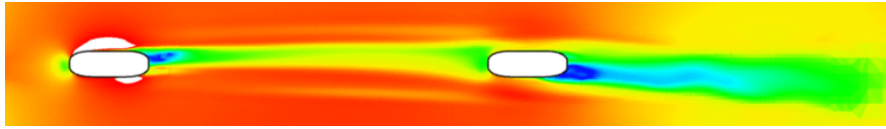
Figure 6.7: Magnitude of V for rotating wheels showing smaller vortex shedding

Due to the rotation of the wheels, the vortex shedding amplitude is reduced by 95.85%. The vortex shedding frequency lowers with 7.99Hz, which is a lowering of 38.52%. This difference in vortex shedding will be the main contributor to the difference in drag between stationary and rotating wheels.

6.4.2 Skin friction drag

On figure 6.8 the drag is divided into the viscous (skin friction) and inviscid (pressure) drag for the rotating wheels. On figure 6.9 the same is shown for the stationary wheels. The x-axis represents the time steps of the unsteady simulations.
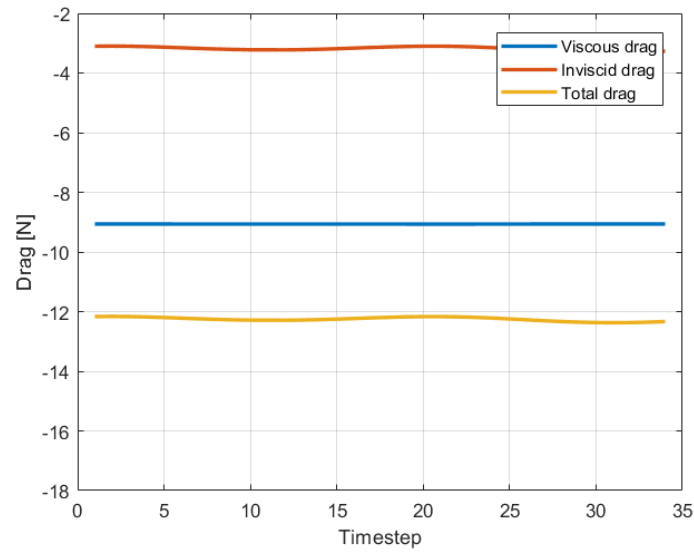
Figure 6.8: Viscous and inviscid drag for rotating wheels
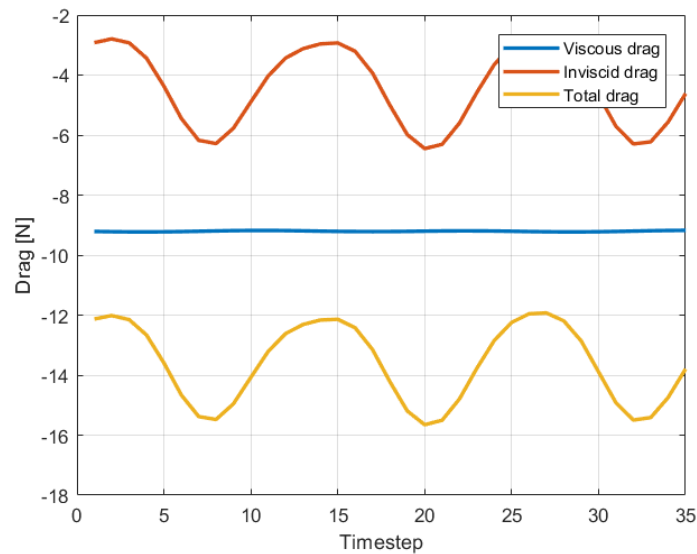
Figure 6.9: Viscous and inviscid drag for stationary wheels

Note: the direction of the force is taken in the same direction as the driving direction. Thus, a negative force means an opposite, counteracting force for the car.

As can be seen on figures 6.8 and 6.9, the viscous drag shows only very small fluctuations compared to the inviscid drag. For the stationary wheels, the viscous drag fluctuates between 9.17 and 9.23N. For the rotating wheels, the viscous drag is constant at approximately 9.06N. Thus, the rotation only has a small influence on the skin friction drag. This is because the main contributor to the skin friction drag is the shell of the car which has a big surface (approximately 9N skin friction drag). The rotation of the wheels will not alter the flow going over the shell. The small difference in skin friction drag between rotating and stationary wheels comes from the change of the flow underneath the car. As described in section 6.4.1, the flow with stationary wheels will be more turbulent behind the wheels. This turbulent flow will cause more skin friction at the parts close to the wheels, like the wheel housings. Nevertheless, the effect of rotation on the skin friction drag will be negligible compared to the effect of rotation on the pressure drag.

6.4.3 Pressure drag

As can be seen on figures 6.8 and 6.9, the inviscid (pressure) drag shows significant differences between the rotating and stationary wheels. This is because the shell of the car is very stream-lined and thus optimised to have a very low pressure drag. Therefore, the wheels will have a relatively big influence on the pressure drag. Changes in drag due to the rotation of the wheels will be noticeable. On figure 6.10 and 6.11, the data of the simulations are displayed. Figure 6.10 shows the data for the stationary wheels. The top left subfigure shows the data for the front wheel. The top right one for the back wheel. The bottom subfigure shows the data for the wheels and the shell of the car. On figure 6.11 the same is shown for the rotating wheels. Next, table

6.5) containing the most relevant data is shown.
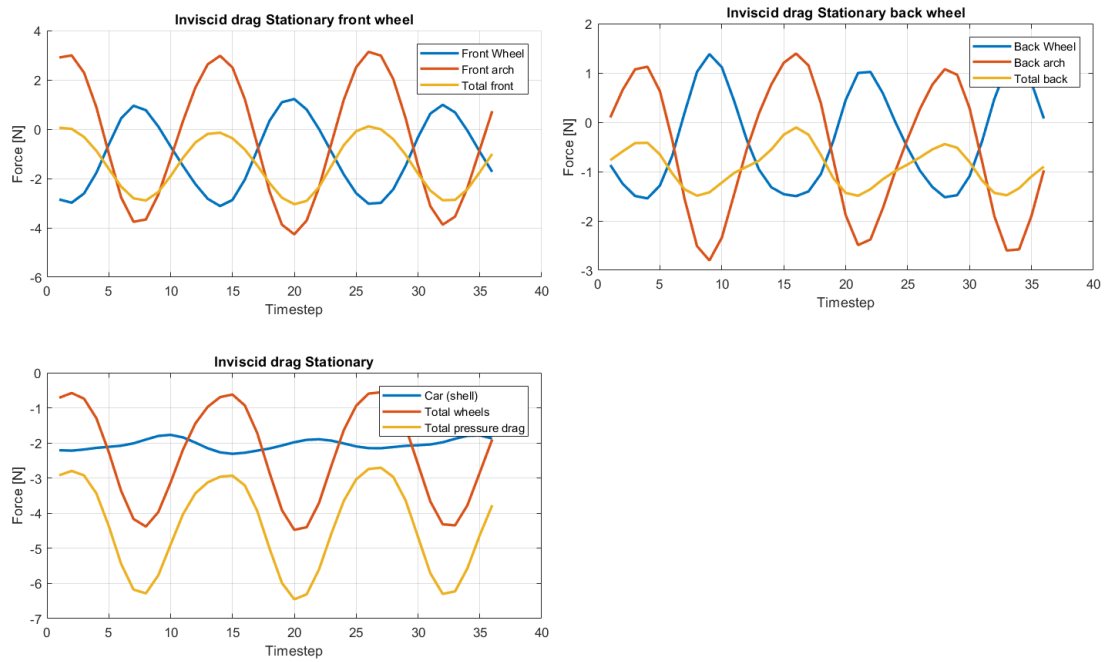
Figure 6.10: Inviscid drag stationary wheels
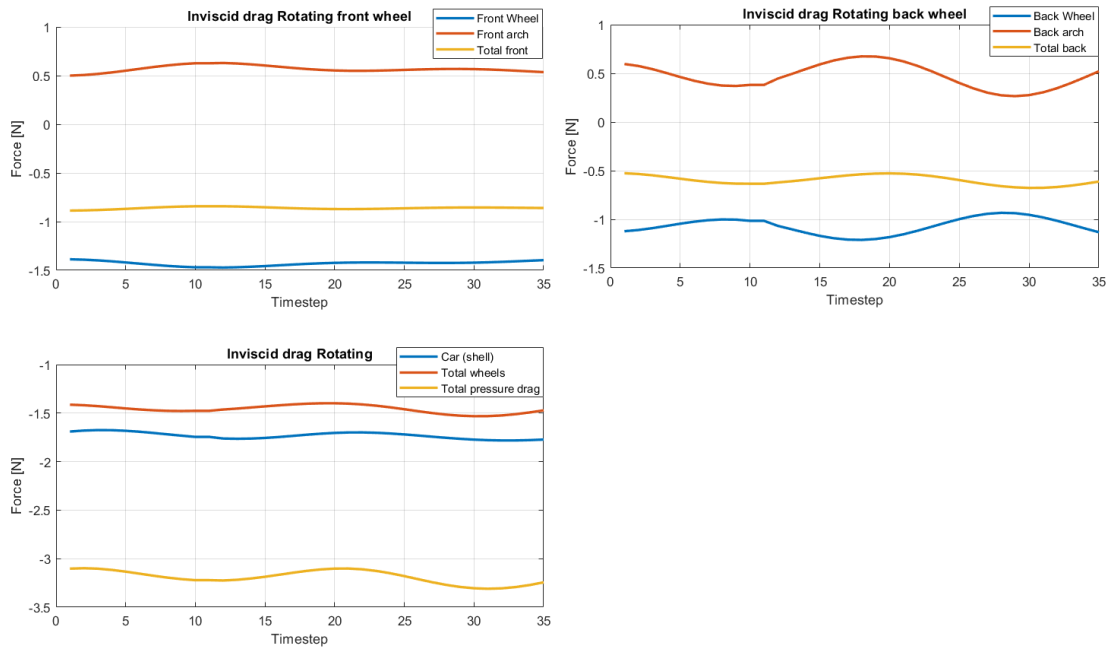
Figure 6.11: Inviscid drag rotating wheels

	Stationary [N]	Rotating [N]
Avg drag shell	2.04	1.73
Max drag shell	2.31	1.78
Min drag shell	1.77	1.68
Avg drag wheels	2.51	1.47
Max drag wheels	4.47	1.53
Min drag wheels	0.56	1.40
Avg total pressure drag	4.58	3.20
Max total pressure drag	6.45	3.31
Min total pressure drag	2.70	3.10

Table 6.5 Pressure drag values

From these figures and table, the following conclusions can be made:

1. As seen in section 6.4.1, the stationary wheels cause vortex shedding whereas rotating wheels suppress it. This will mainly have an effect on the pressure drag difference. The vortex shedding will create a bigger and fluctuating low-pressure zone behind the stationary wheels. Therefore, the drag of the stationary wheels shows bigger fluctuations and a higher average value than the rotating wheels.
   Also, due to the vortex shedding suppression, the wake behind the rotating wheels is narrower as can be seen on figure 6.6 and 6.7 on vortex shedding. This will improve the flow around the rest of the car [41].

2. The drag of the shell of the car is bigger with the stationary wheels. Also, small fluctuations can be noticed in the drag of the shell in both scenarios. They are in phase with the vortex shedding. This implies that the vortex shedding behind the wheels will have a small impact on the drag of the shell. The impact will be in the wake behind the wheelhouse which is close to the wheels. This wake will be larger and fluctuate slightly because of the vortex shedding of the wheels. Due to the bigger vortex shedding of the stationary wheels, the impact will be bigger. Overall, the impact on the shell of the car itself is relatively small and the differences are mainly at the wheels themselves.

3. The pressure drag of the rotating wheels is in the same order of magnitude as the pressure drag of the shell. For the stationary wheels the drag is even higher than the shell. It is therefore very important not to neglect the wheels when studying/optimising the pressure drag.

4. In both scenarios (stationary and rotating), the front wheels have a higher pressure drag than the back wheels. This is against the expectations because the back wheels show larger amplitudes in vortex shedding. This can be seen in the previous pictures (6.6 and 6.7). There are two reasons for this behaviour. The first one can be found in the stagnation pressure. The stagnation pressure at the back wheels is lower because the flow has

slowed down due to the front wheels. Also the flow is not perpendicular to the back wheels because of the vortex shedding of the front wheels.

The second reason is in the low-pressure zone behind the wheels due to the vortex shedding. On figure 6.12, the pressure contour for stationary wheels at one time step is shown. The front wheel is shown at the left-hand side, the back wheel at the right-hand side. Although the wake is bigger behind the back wheels, the pressure at the wheels themselves is lower at the front wheels.

Figure 6.12: Pressure contour of stationary wheels

Thus, the front wheels have a higher stagnation pressure at the front and a lower pressure at the back than the back wheels. This will result in a higher drag for the front wheels.

5. The two top subfigures of figure 6.8 and 6.9 divide the drag of the wheels and the arches. As can be seen, the drag of the wheels and the arches are in anti-phase. This is logical because the wheel and the arch form an action-reaction pair. For example, if the pressure at the front between the arch and wheel is high, it will push the wheel backwards and the arch forwards. Resulting in an opposite drag force for both. The drag forces are not equal in size because the bottom of the wheel is not encapsulated by the arches. Figure 6.13 shows the non-encapsulated area and shows the example of opposite forces for the wheel and arch.
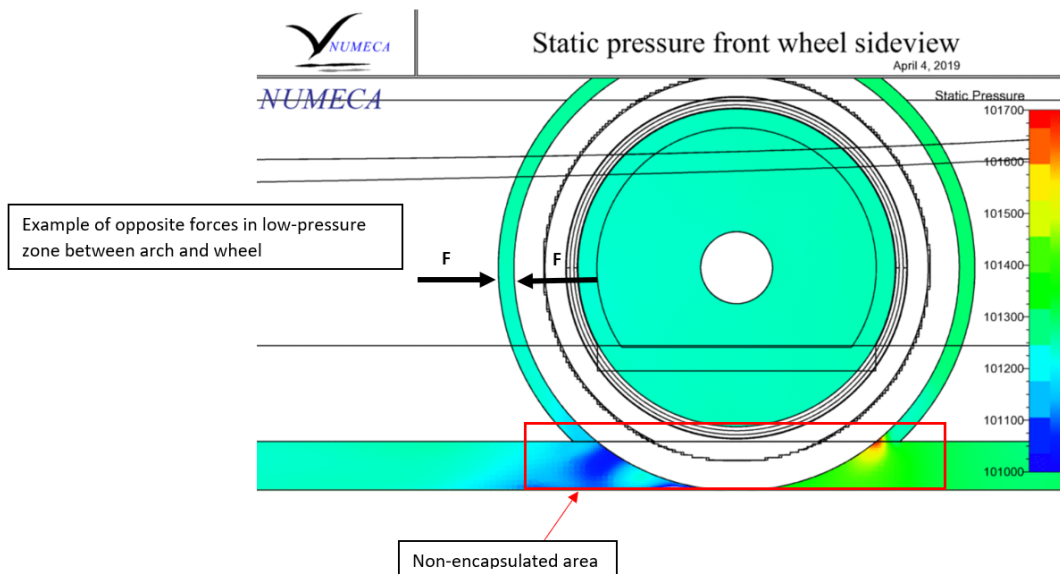
Figure 6.13: Static pressure front wheel side view

With the rotating wheels, the forces on the wheels stay negative and the forces on the arches stay positive. This implies that the pressure distribution inside the arch stays the same, meaning a high pressure at the front of the wheel and a low pressure at the back of the wheel. This is because there is almost no vortex shedding and thus no oscillating pattern. This can be seen on figure 6.14.

(a) Time step 5
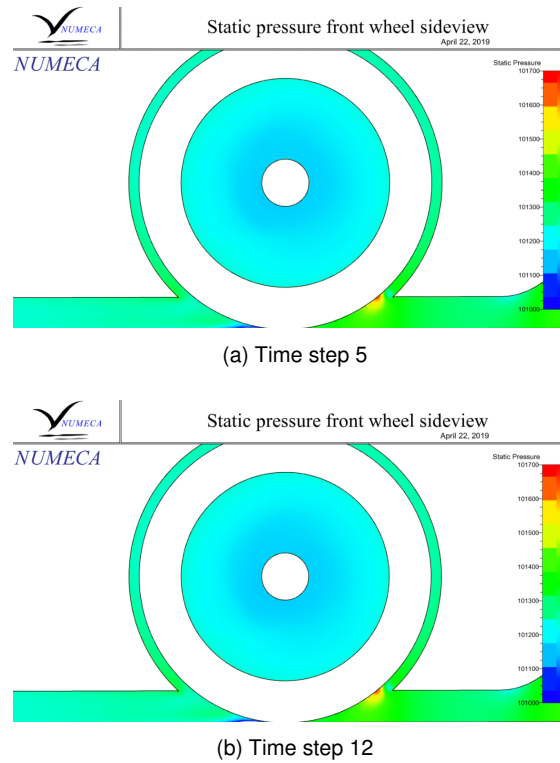
(b) Time step 12

Figure 6.14: Pressure contour between wheel and arch at different time steps (rotating)

With the stationary wheels, the forces on the arches and the wheels both fluctuate to positive and negative drag values. This is because of the strong vortex shedding, the pressure distribution inside the arches also fluctuates. This can be seen on figure 6.15.
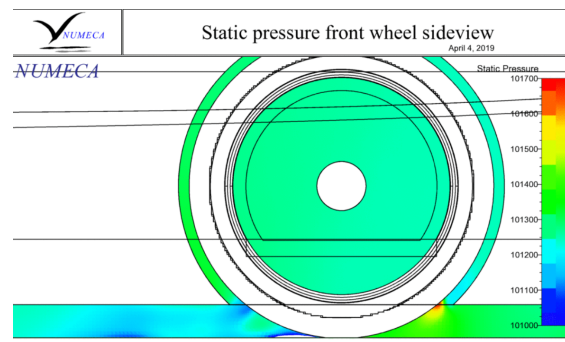
(a) Time step 5: low pressure at right-hand side between wheel and arch
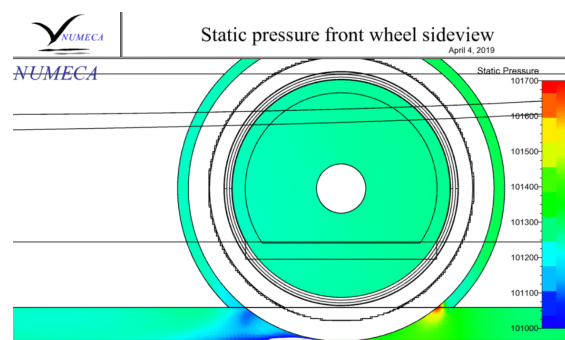
(b) Time step 12: low pressure at left-hand side between wheel and arch

Figure 6.15: Pressure contour between wheel and arch at different time steps (stationary)

6. As previously described, vortex shedding is taking place with the stationary wheels. Because of the vortex shedding, fluctuating drag patterns arise behind the wheels. For the rotating wheels, this effect is very small. As described in the research of Pogosov [56], two stationary cylinders behind each other could have a different vortex shedding frequency in which the front cylinder has the highest frequency of the two. This could also be the case for the stationary wheels behind each other. On figure 6.16 the drag of the car in function of the time steps is shown, as well as the Fourier transform of this time signal. There is a beat (see section 2.3) pattern visible (especially in the beginning) but this is a very slow beat. This could be because of the small difference in frequencies between the wheels. There are two dominant frequencies visible in the Fourier transform, which are 21.01Hz (front wheel) and 20.62Hz (back wheel). These frequencies are situated close to each other. Therefore, the enveloping frequency of the possible beat would be 0.305Hz (see equation 2.12). The simulation has 655 timesteps, which results in a spectral resolution of 0.396Hz for the Fourier transform, which is too high to prove if the two frequencies of the wheels are really two different frequencies. Therefore, it can not be validated if beat is a transient phenomenon or that it is still present at the end of the simulation. A research into the existence of beat for the stationary solar car tyres could be a subject for further research. One should also note that the amplitude of the drag generated by front and back

wheel will be different which makes that the beat signal will not go to zero (if beat would be present).
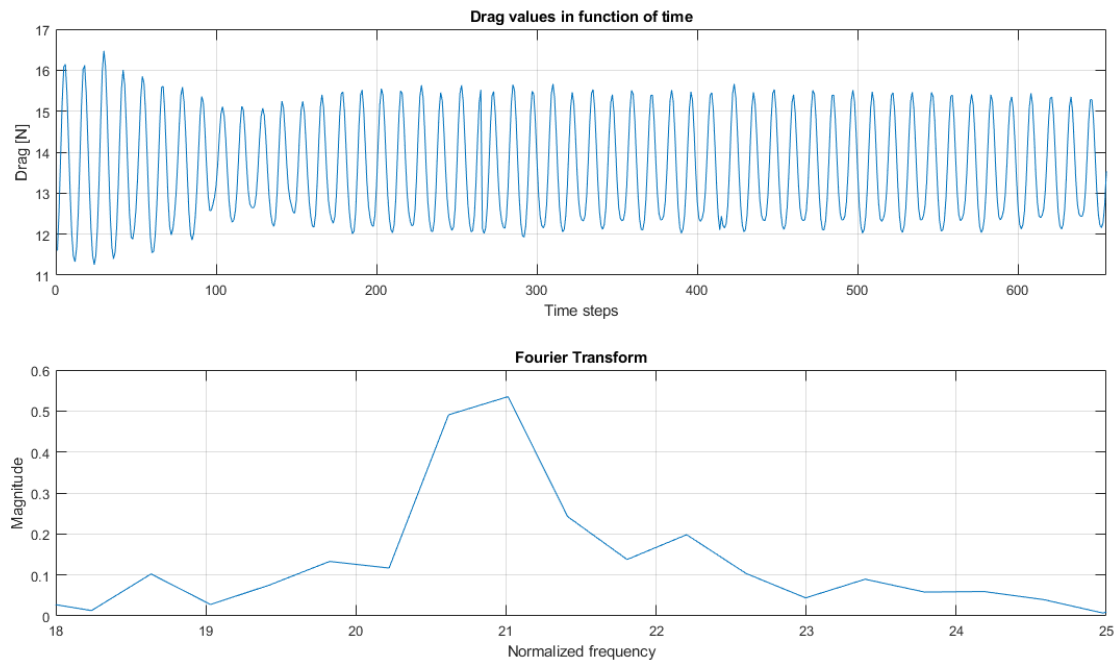
Figure 6.16: Drag values in function of time and its Fourier transform

General conclusion

The total pressure drag is lower for the rotating wheels than for the stationary wheels. This is due to the phenomenon of vortex shedding which is responsible for a higher drag [12, 13, 14, 15]. The amplitude of the sinusoidal drag is bigger for the stationary wheels, which leads to the conclusion that vortex shedding is more present for stationary wheels. Rotating wheels produce a narrower wake which improves the drag for the components around and behind the wheels.

Beat happens with the stationary wheels as an effect of a slight difference in vortex shedding frequency between the two wheels. Therefore, there is not only a fluctuating drag due to vortex shedding but the drag also fluctuates at a lower frequency due to the beat. It is still unclear if this beat generation is transient behaviour or not.

6.4.4   Model for drag of rotating wheels

In the previous section, the origin of the drag differences between stationary and rotating wheels is explained. In this section, a model will be described that will be used to estimate the drag of the car with rotating wheels based on data of stationary wheels. The data of the stationary wheels comes from the wind tunnel, which is not able to let the wheels rotate. Previous simulations were all done at a speed of 90 km/h and the model will be made for this speed.

Extrapolate values to full car

All simulations have been done on a half car. This is to reduce computational times. Based on previous research of the Solar Team, these values will be extrapolated to a full car. The extrapolation is needed for the model to have the right relative influence of the wheels. For this, the following data is needed:

- Drag of canopy: the side that is simulated in this research does not contain the canopy. Therefore the drag of the canopy has to be added. This value is 5.52 N.

- Drag of right-hand side wheelhouse: in this research the left-hand side wheelhouse is used. The wheelhouse at the right-hand side is wider because the driver sits at this side. Therefore it will have a different drag value. From previous research, it is concluded that, because of a high positive pressure at the back of the right-hand side wheelhouse, the drag will be lower. This is against expectations but might be possible due to influences from the canopy. The difference in drag that has to be subtracted is 1.24 N.

To estimate the drag of the full car, the drag from this research is doubled (because of the half car) and the differences in drag due to the right-hand side wheelhouse and the canopy are taken into account. This yields to the following results as shown on figure 6.17 and in table 6.6.
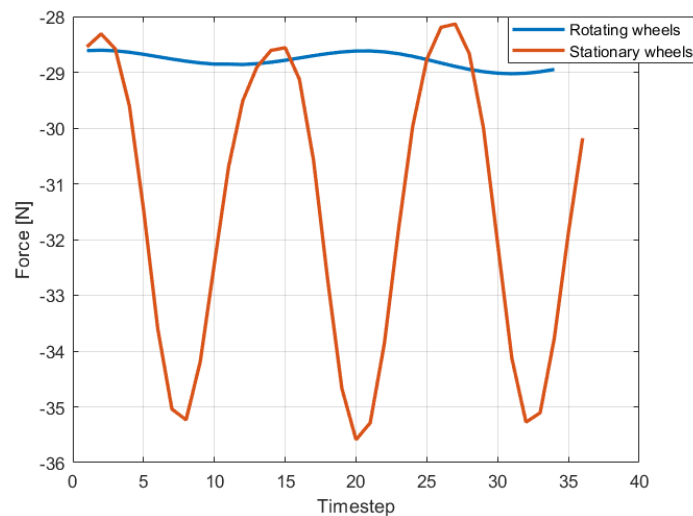
Figure 6.17: Total drag rotating and stationary wheels

	Stationary	Rotating
Avg drag [N]	31.86	28.82
Max drag [N]	35.59	29.03
Min drag [N]	28.13	28.61

Table 6.6 Total extrapolated drag for stationary and rotating wheels

Model

Now that all the data is available, the relative impact of the rotating wheels can be calculated. In table 6.7 the difference in drag going from stationary to rotating wheels for different components can be seen. Note that these are also extrapolated values from a half to a full car. The values are based on the absolute values found in table 6.6 and section 6.4.2 and 6.4.3.

	Change [N]	Change [%]
Avg drag **shell**	-0.9	-3.59
Avg drag **wheels**	-2.08	-41.43
Avg **viscous** drag	-0.27	-1.33
Avg **inviscid** drag	-2.75	-27.91
Avg **total** drag	-3.04	-9.54
Max total drag	-6.6	-18.43
Min total drag	+0.45	+1.68

Table 6.7 Change in drag (stationary to rotating) for extrapolated full
car

From table 6.7 the following can be concluded:

- The biggest change in drag can be seen in the inviscid (pressure) drag. This is mainly because of the wheels which are responsible for the vortex shedding.

- The viscous drag does not change very much. This is because the main contributor of the viscous drag, namely the top shell, is not influenced by the wheels.

- To transform the total drag of the car from stationary to rotating wheels, the average drag lowers with 9.54%. The minimum value of the total drag increases with 1.68% and the maximum value lowers with 18.43%. Due to the big fluctuations with the stationary wheels and the steady behaviour of the rotating wheels, there is a big difference between the minimum and maximum values.

It has to be noted that these percentages are only valid for a velocity of 90 km/h. Because the drag is proportional to v^2, these percentages will not be the same at other velocities. Using equation 6.5, the percentages can be transformed:

$$F_{drag,new} = \frac{F_{drag,old} \cdot u_{new}^2}{u_{old}^2}$$
(6.5)

It is not yet clear if the vortex shedding is also proportional to v^2 in the interval of driving velocities of the solar car. So, simulations at other velocities should be performed to validate the equation, this could be done in a future research.

6.5   Flow field visualisation

Another part of this research is to visualise and describe the flow field caused by the rotating wheels. Up till now, this flow field is unknown because the wheels were neglected in previous simulations of the Solar Team. When the flow field of the rotating wheels is known, optimisations on the wheels and wheel arches can be suggested. Therefore, this section will describe the flow field between the wheel and arch for the rotating wheels. Also, the flow in front and behind the wheels is visualised. On figure 6.18, the overall streamlines caused by the wheels are shown. It has to be noted that on most of the figures that are shown in this chapter, only the wheels are visible. The arches and the car are made transparent to improve visibility.
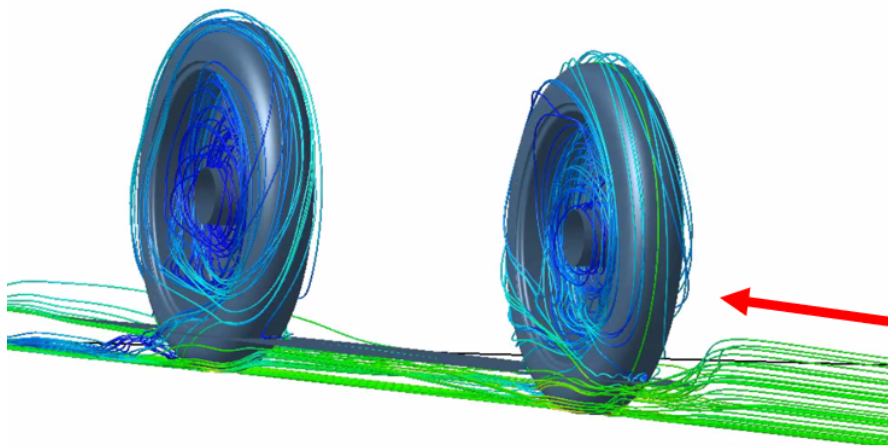
Figure 6.18: Velocity streamlines around wheels

The flow between the wheel and the arch is mostly a stable flow. Only at the lower front and back of the wheels, where the flow inside the arches interacts with the free stream flow, unstable regions exist. On figure 6.19a, it can be seen that there is a recirculation zone at the front of the wheel and the wheel arch. This is because there are two streams of flow coming together: the first one is the free stream flow coming from the front of the car. The second one is the flow between the wheel and the wheel arch which is transported because of the rotation of the wheels. On figure 6.19b, these flows are shown.
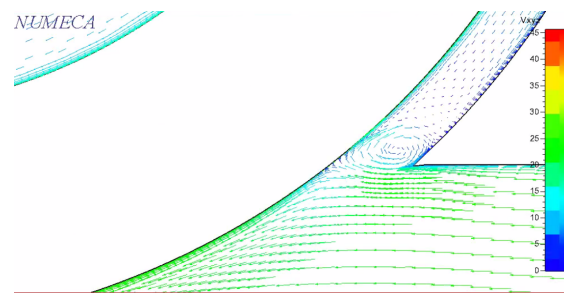
(a) Velocity front wheel
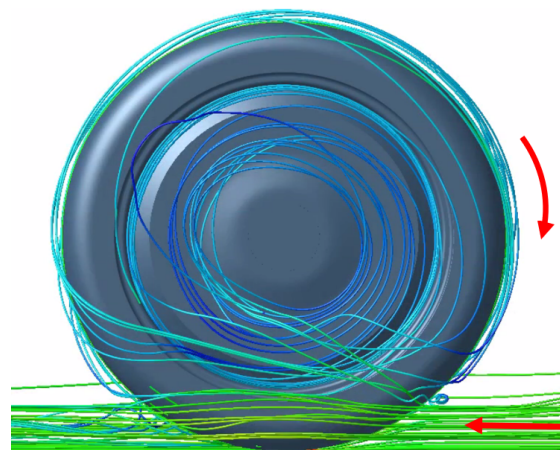
(b) Velocity streamlines front wheel

Figure 6.19: Velocity between wheel and wheel arch front wheel

On figure 6.19b, it can also be seen that the flow does not enter the wheel from the front. The flow goes around the wheel and goes up at the back of the wheel where it is transported due to the rotation. The same is valid for the back wheel.

The eddies behind the back wheel can be seen on figure 6.20. On the figure, the left and right-hand side of the back wheel are shown. The flow direction is indicated with the red arrow. The eddies arise due to vortex shedding, which is thoroughly described in section 6.4.1. Also, flow from inside the wheel arch, which is at a relatively low velocity, enters the free stream flow and causes the eddies to form.
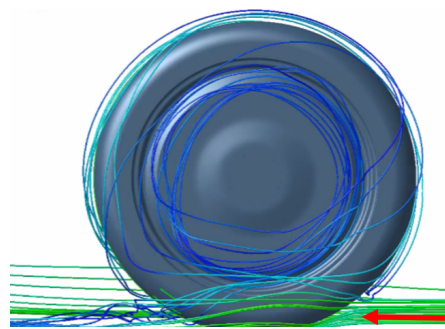
(a) Right-hand side back wheel
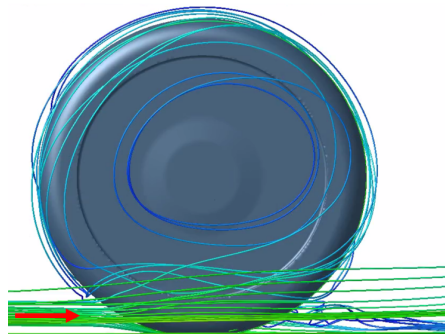
(b) Left-hand side back wheel

Figure 6.20: Velocity streamlines back wheel

On figure 6.21, the velocity streamlines at the rear side of the back wheel are shown to illustrate the eddies at a given time step.
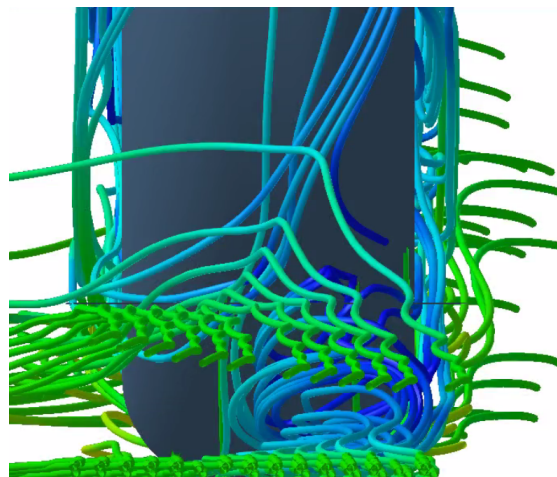
Figure 6.21: Rear side of back wheel

The pressure inside the wheel arch is uniformly distributed and is around 101200Pa at the rim and 101250Pa between the wheel and the arch, as can be seen on figure 6.22. As described in section 6, at the front of the wheels the pressure is higher due to the stagnation of the flow.

Behind the wheels, the pressure is lower due to the recirculation zones. The stagnation pressure at the back wheel is lower because the flow has already slowed down due to the front wheels.

(a) Pressure distribution at back rotating wheel

(b) Pressure distribution at front rotating wheel

(c) Scale of static pressure values
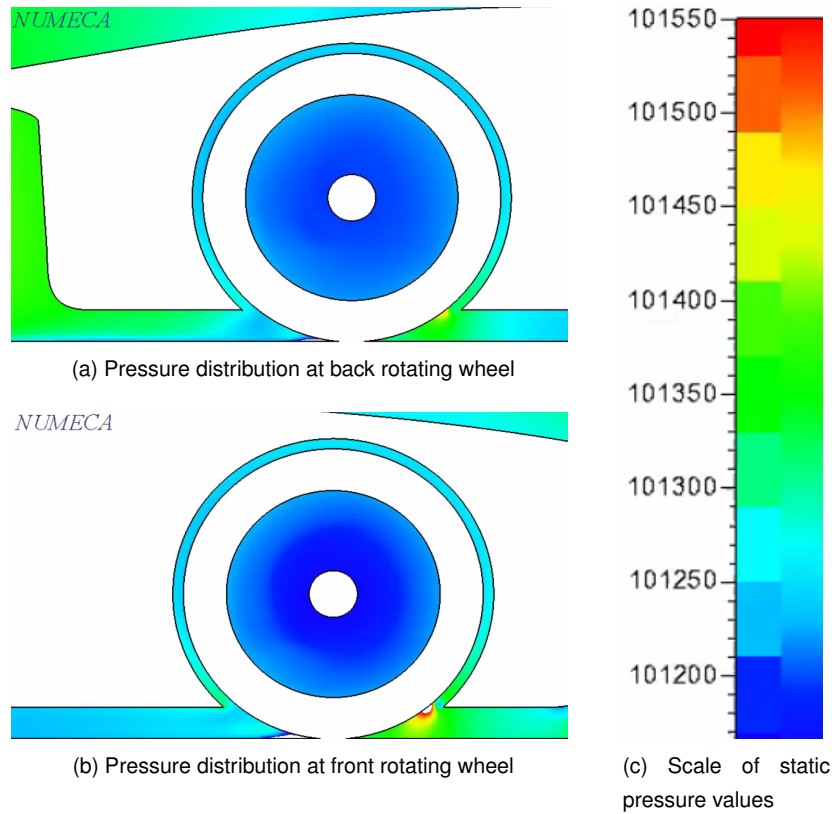
Figure 6.22: Pressure distribution of rotating wheels

At last, the velocity profile inside the arch is described. On figure 6.23, the velocity between the wheel and arch can be seen. At the tyre surface, the velocity of the flow is 25 m/s due to the no-slip condition. The velocity at the arch surface is 0 m/s. In the middle of the two, the velocity is around 11 m/s. The boundary layers do not interact with each other with the current spacing between wheel and arch.
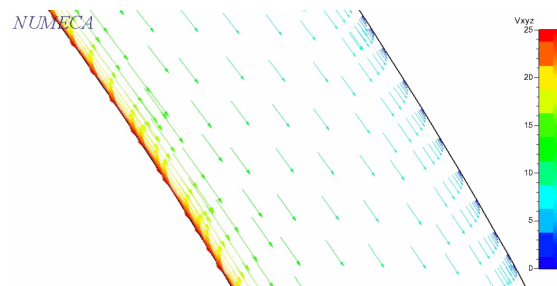
Figure 6.23: Velocity between wheel and arch

Chapter 7

Conclusions and further research

Conclusions

This research made use of the unsteady RANS equations with a k-ω SST turbulence model. Certain simplifications were made to the geometry to reduce the necessary computational effort (closing the gap between the car and the arches so no flow could enter the car, simplifying the rim,...). Also, only half of the car was simulated. For this case, this still led to viable results to draw conclusions from, in a realisable time span. To mimic the rotation of the wheels, it was opted to use a moving wall boundary condition. As stated in the validation phase (6.2), this method is suitable because of the closed rim geometry of the solar car rims. Also, it is a time-efficient method to simulate rotation. When simulating the solar car with the wheels, it is advised to use rotating wheels instead of stationary wheels. This is off course based on the interest whether the real-life drag or wind tunnel drag has to be modelled. Nevertheless, the preference goes to the rotating wheels because the stabilisation time of the simulation for rotating wheels is much shorter. From section 6.3, it can be seen that the rotating wheels only need about 10% of the time needed for stationary wheels to stabilise.

As expected, the rotating wheels lower the drag of the car in comparison to stationary wheels. This is due to the phenomenon of vortex shedding. The stationary wheels show vortex shedding, whereas rotating wheels mostly suppress it. Therefore, the drag of the wheels themselves lowers significantly (41.43%). Also, the rotation of the wheels creates a narrower wake behind the wheels. Due to this, other parts around and behind the wheels experience less drag. As a consequence, the total drag of the car drops with 9.54% for a velocity of 90 km/h. This is mainly in the pressure drag because the vortex shedding influences the low-pressure wake behind the wheels and the car. The viscous drag does not change very much (lowers 1.33%). This is because the main contributor to the viscous drag, namely the top shell, is not influenced by the wheels.

Another part of this research was the visualisation of the flow field of the rotating wheels as this was unknown up till now. This was done for the current geometry of wheels and arches. From this followed, that inside the arches the flow is stable. In the front and in the back of each wheel, instabilities exist. These come from the oscillations caused by the vortex shedding as well as the interaction of flow inside the arches with the free stream flow underneath the car.

The results in this research were all based on simulations with a moving ground, namely station- ary wheels with a moving ground and rotating wheels with a moving ground. This had been done to isolate the effect of the rotation of the wheels and to only have one changing variable, keeping the boundary conditions the same. The case with the stationary wheels and moving ground is not a real-life case. Therefore, the model described in this research, for transforming the drag of stationary wheels to rotating wheels could be improved.

Further research

This research was the first one including the wheels into the simulation of the drag of the Solar Car. Therefore, different simplifications were made, which makes that there is room for further research. The current research can form the basis for the following recommended domains:

- Further research could be done about the geometry of the components around the wheels. The adaptations can be based on the current flow field, described in this research, to improve the overall drag.

- Further research could be done into the effects of different simplifications made for the simulations:

    - Taking the grooves of the tyres into account
    - Keeping the gap between arch and shell of the car so flow can enter the car
    - Simulating the full car instead of the half car

- The current model could be extended to a model to transform wind-tunnel conditions to driving conditions, by doing further research on stationary wheels with a stationary ground boundary condition. The current model could also be improved by validating it at other velocities (generalisation).

- At last, research into the existence of beat for the stationary solar car tyres could be inter- esting, as this could be useful for wind tunnel measurements.

Bibliography

[1] E. Vandervelpen and J. Uten, "Testing of turbulence models for the aerodynamic simulations of a solar car," 2018.

[2] C. Fu, M. Uddin, and A. C. Robinson, "Turbulence modeling effects on the cfd predictions of flow over a nascar gen 6 racecar," *Journal of Wind Engineering and Industrial Aerodynamics*, vol. 176, pp. 98 – 111, 2018.

[3] W. S. Challenge, "2019 regulations, 13-20 oct 2019." `https://www.worldsolarchallenge.org/files/2272_2019_bwsc_regulations_release_version_3.pdf`, October 2018.

[4] NUMECA, "Numeca: A new wave in fluid dynamics," 2019.

[5] M. A. T. P. P. J. Fox, Robert W, *Introduction to fluid mechanics (6th ed.)*. Hoboken: Wiley, 2004.

[6] M. Vanierschot, "Computer aided vehicle design: Aerodynamics." Powerpoint, 2018.

[7] D. P. Holmes, "Mechanics of materials: Stress transformation mechanics of slender structures — boston university," Mar 2015.

[8] N. Halle, "Boundary layer." `https://www.grc.nasa.gov/www/k-12/airplane/boundlay.html`, May 2015.

[9] W. Frei, "Which turbulence model should i choose for my cfd application?." `https://www.comsol.com/blogs/which-turbulence-model-should-choose-cfd-application/`, July 2017.

[10] T. L. CFD, "Turbulence part 3 - selection of wall functions and y+ to best capture the turbulent boundary layer." `https://www.computationalfluiddynamics.com.au/turbulence-part-3-selection-of-wall-`, april 2013.

[11] aerospaceengineeringblog, "Boundary layer separation and pressure drag." `https://aerospaceengineeringblog.com/boundary-layer-separation-and-pressure-drag`, October 2016.

[12] R. D. Henderson, "Details of the drag curve near the onset of vortex shedding," *Physics of Fluids*, vol. 7, no. 9, pp. 2102–2104, 1995.

[13] B. Guido, *Vortex shedding from bluff bodies*, pp. 61 – 95. Balkema, Rotterdam, 01 1998.

[14] A. Villegas and F. Diez, "Effect of vortex shedding in unsteady aerodynamic forces for a low reynolds number stationary wing at low angle of attack," *Journal of Fluids and Structures*, vol. 64, pp. 138 – 148, 2016.

[15] S. C. Yen and C. W. Yang, "Flow patterns and vortex shedding behavior behind a square cylinder," *Journal of Wind Engineering and Industrial Aerodynamics*, vol. 99, no. 8, pp. 868 – 878, 2011.

[16] A. Kolmogorov, "The local structure of turbulence in incompressible viscous fluid for very large reynolds' numbers," *Akademiia Nauk SSSR Doklady*, vol. 30, pp. 301–305, 1941.

[17] B. Cushman-Roisin, *Environmental Fluid Mechanics*. Dartmouth, 2018.

[18] M. T. L. E. Mollo-Christensen, *Turbulence and Random Processes in Fluid Mechanics (2nd ed.)*. Cambridge University Press, 1992.

[19] V. Fichet, "Modélisation de la combustion du gaz naturel par réseaux de réacteurs avec cinétique chimique détaillée," Master's thesis, Ecole Centrale Paris, Paris, 2008.

[20] N. Foroozani, *Numerical Study of Turbulent Rayleigh-Benard Convection with Cubic Confinement*. PhD thesis, Universita degli studi di Trieste, 04 2015.

[21] A. Bakker, "Lecture 10 - turbulence models," applied computational fluid dynamics, Dartmouth College, 2002-2006.

[22] J. O. Hinze, *Turbulence*. New York : MacGraw-Hill, 1975.

[23] S. IP, "4.14.3. scalable wall functions." `https://www.sharcnet.ca/Software/Ansys/16.2.3/en-us/help/flu_th/flu_th_scale_wf.html`, June 2015.

[24] T. Lajos, "Basics of vehicle aerodynamics," tech. rep., University of Rome La Sapienza, 2002.

[25] J. Edgar, "Analysing road car drag." `http://www.autospeed.com/cms/article.html?&title=Analysing-Road-Car-Drag&A=113227`, 2009.

[26] BoH, "Drag (physics)." `https://commons.wikimedia.org/w/index.php?curid=6742156`, October 2009.

[27] SKYbrary, "Friction drag." `https://www.skybrary.aero/index.php/Friction_Drag`, July 2017.

[28] R. J. Adrian, "Drag of blunt bodies and streamlined bodies," tech. rep., Princeton University, 2019.

[29] J. L. Monteith and M. H. Unsworth, "Chapter 9 - momentum transfer," in *Principles of Environmental Physics (Fourth Edition)* (J. L. Monteith and M. H. Unsworth, eds.), pp. 135 – 150, Boston: Academic Press, fourth edition ed., 2013.

[30] A. Dorsey, "Skin friction," tech. rep., Virginia University, 1997.

[31] P. Friend, "aerodynamic resistance and the use of aerodynamic coefficients." `http://www.pilotfriend.com/training/flight_training/aero/aero_res.htm#r`, 2019.

[32] T. Hobeika, S. Sebben, and C. Landstrom, "Investigation of the influence of tyre geometry on the aerodynamics of passenger cars," *SAE Int. J. Passeng. Cars - Mech. Syst.*, vol. 6, pp. 316–325, 04 2013.

[33] ANSYS, "3.2 sliding mesh theory." `http://www.afs.enea.it/project/neptunius/docs/fluent/html/th/node37.htm#sec-slide-intro`, January 2009.

[34] S. Diasinos, T. J. Barber, and G. Doig, "The effects of simplifications on isolated wheel aerodynamics," *Journal of Wind Engineering and Industrial Aerodynamics*, vol. 146, pp. 90 – 101, 2015.

[35] P. Lesniewicz, M. Kulak, and M. Karczewski, "Aerodynamic analysis of an isolated vehicle wheel," *Journal of Physics: Conference Series*, vol. 530, p. 012064, 08 2014.

[36] K. M and B. J, "Performance of three turbulence models in 3d flow investigation for a 1.5-stage turbine," *TASK Quarterly*, pp. 185–195, 2008.

[37] S. K and B. J, "Numerical analysis of the flow around a cylinder," *CMP*, pp. 53–66, 2010.

[38] K. K and K. W, "Verification of the numerical model of the viscous gas flow within a centrifugal compressor stage," *Nauchno-Technicheskie Vedomosti SPbGPU*, pp. 329–334, 2011.

[39] V. Veeraraghavan, "Aerodynamics of a rotating wheel in a wheelhouse: A numerical investigation using les," 10 2017.

[40] J. Fabijanic, "An experimental investigation of wheel-well flows," in *SAE Technical Paper*, SAE International, 02 1996.

[41] A. Wäschle, "The influence of rotating wheels on vehicle aerodynamics - numerical and experimental investigations," in *SAE Technical Paper*, SAE International, 04 2007.

[42] "Tread pattern anatomy." `http://www.tireprofiles.com/tread-pattern-anatomy/`, January 2019.

[43] N. Hawinkel, "Aerodynamic analysis of punch one powertrain solar car," 2016.

[44] T. Craft, "Near-wall modelling," tech. rep., The University of Manchester, 2018.

[45] "Understanding the contact patch." `https://www.discounttire.com/learn/contact-patch`, May 2019.

[46] Unknown. `http://paws.kettering.edu/~amazzei/tire_calculator.html`, 2008-2009.

[47] J. Reimpell, H. Stoll, and J. W. Betzler, "Tyres and wheels," in *The Automotive Chassis (Second Edition)*, pp. 86 – 148, Oxford: Butterworth-Heinemann, second ed., 2001.

[48] I. SAS IP, "Skewness." `https://www.sharcnet.ca/Software/Ansys/17.0/en-us/help/wb_msh/msh_skewness.html`, December 2015.

[49] S. IP, "15.3.2. measures of mesh quality." `https://www.sharcnet.ca/Software/Ansys/16.2.3/en-us/help/cfx_mod/i1323480.html`, June 2015.

[50] NUMECA, "Show mesh quality." `https://portal.numeca.be/docs/OMNIS/Default.htm#_url/MESH/show-mesh-quality.htm%3FTocPath%3DOMNIS%25E2%2584%25A2%2520tools%7CMesh%2520Generation%7C_____4`, March 2019.

[51] A. Stoukov, "Strouhal number," 2001-2002.

[52] NUMECA, "k-ω (m-sst) turbulence model," 2019.

[53] P. Roache, "Perspective: A method for uniform reporting of grid refinement studies," *Journal of Fluids Engineering-transactions of The Asme - J FLUID ENG*, vol. 116, pp. 405–413, 09 1994.

[54] J. W. Slater, "Examining spatial (grid) convergence." `https://www.grc.nasa.gov/www/wind/valid/tutorial/spatconv.html`, July 2008.

[55] C. J. Roy, "Grid Convergence Error Analysis for Mixed-Order Numerical Schemes," *AIAA Journal*, vol. 41, pp. 595–604, april 2003.

[56] M. Pogosov, "Cfd simulations of flow around the tandem cylinders close to the seabed," Master's thesis, University of Stavanger, Stavanger, 2016.

Appendix A

Electronical appendices

All appendices are electronically available on request and will not be provided in this text book. The available appendices are:

- Geometry files (CAD)

- Detailed mesh configuration file

- Detailed solver configuration file

- MATLAB code used for post-processing

- Results of unsteady simulations in GIF format

- Output files in Fine^{TM}/Open solver 8.1 format

FACULTY OF ENGINEERING TECHNOLOGY
GROUP T LEUVEN CAMPUS
Andreas Vesaliusstraat 13
3000 LEUVEN, België
tel. + 32 16 30 10 30
fet.groupt@kuleuven.be
www.fet.kuleuven.be